

Constraining the past X-ray luminosity of AGN in clusters of galaxies: the role of resonant scattering

S.Yu. Sazonov^{1,2}, R.A. Sunyaev^{1,2} and C.K. Cramphorn¹

¹Max-Planck-Institut für Astrophysik, Karl-Schwarzschild-Str. 1, 85740 Garching bei München, Germany

²Space Research Institute, Russian Academy of Sciences, Profsoyuznaya 84/32, 117997 Moscow, Russia

Received ; accepted

Abstract. Only a small fraction of galactic nuclei in the nearby universe are luminous, while most of them are currently dim. We investigate the feasibility of constraining the X-ray luminosity in the recent past (up to $\sim 10^6$ years ago) of the nucleus of a cluster dominant galaxy by measuring the contribution of scattered nuclear radiation to the surface brightness of the intracluster gas dominated by thermal emission. We show that resonance X-ray lines present advantage over the continuum near the lines, because the relative contribution of scattered radiation is typically larger in the line case by a significant factor of the order of 3–10. As an example, we estimate the level of constraints that could be derived from future fine spectroscopic observations on the past X-ray luminosity of the nearby M87 and Cygnus A active galaxies. For comparison we show that already available XMM-Newton and Chandra data on the continuum emission from the X-ray haloes around these galaxies enable obtaining an order of magnitude weaker upper limits on their past luminosity.

A similar method can be applied to distant powerful quasars (at redshifts $z \gtrsim 1$) if they have cluster-like gaseous coronae, as suggested by Rosat and Chandra observations of active galaxies at $z \lesssim 1$. Their surface brightness profiles in the X-ray continuum above ~ 10 keV $\gg kT/(1+z)$ (where T is the gas temperature) should be dominated by redshifted scattered radiation from the quasar. Therefore, measurements with the next generation of X-ray telescopes could give information on the lifetime of quasars and parameters of the hot gas around them.

Key words: galaxies: active – quasars: general – scattering – X-rays: galaxies: clusters

1. Introduction

It is commonly believed that active galactic nuclei (AGN) are powered by accretion onto a supermassive black hole. However, a detailed description of this process is still missing. One of the principal obstacles to making a progress

here is that we know very little from observations about the variability of AGN on timescales longer than a few tens of years.

Nuclear variability on the longest timescales up to the Hubble time is expected to be governed by the supply of gas from galactic scales to the central kpc. Such transport can be triggered by mergers and interactions of galaxies (e.g. Hernquist 1989). There are reasons to believe that AGN can be strongly variable on timescales much shorter than the Hubble time. For example, Ciotti & Ostriker (2001) have suggested a mechanism for elliptical galaxies in which an accreting central black hole heats the ambient gas to the point at which the accretion stops, then fueling resumes after the gas has cooled. In this model, strong outbursts during which the AGN luminosity approaches the Eddington critical value can occur every 10^8 – 10^9 years. A similar outburst behaviour but on shorter timescales of typically 10^6 years can result from thermal-viscous instability expected to operate in AGN accretion disks (e.g. Lin & Shield 1986; Mineshige & Shields 1990; Siemiginowska, Czerny & Kostyunin 1996; Burderi, King & Szuszkiewicz 1998). We should also mention tidal disruption of stars by supermassive black holes, which can give rise to rare (every 10^4 – 10^5 years per galaxy), short (months to years) and bright (sub-Eddington) flares (e.g. Lidskii & Ozernoi 1979; Rees 1988).

Since we are unable to explore directly the long-term variability of galactic nuclei, some indirect methods are in need. One feasible way is to observe radiation which was emitted in the past by a galactic nucleus and later on scattered towards us by the interstellar medium. Since the characteristic size of a galaxy is a few tens kpc, we could see the “echo” of previous nuclear activity $\sim 10^5$ years after the central source turned off. This idea has been put forward by Sunyaev et al. (1993) in connection to our Galaxy. Namely, it was suggested that the diffuse, hard X-ray emission observed today in the direction of giant molecular clouds in the central 100 pc of the Milky Way is scattered radiation emitted by Sgr A* in the past. Cramphorn & Sunyaev (2002) have recently elaborated on this

problem and derived upper limits on the X-ray luminosity of Sgr A* during the past 10^5 years.

It seems natural to extend the above approach on elliptical galaxies and in particular cluster cD galaxies. Recent observations with the Hubble Space Telescope and ground-based telescopes have confirmed previous suggestions that 1) powerful low-redshift ($z < 0.5$) AGN are found in luminous and preferentially early-type galaxies (e.g. Bahcall et al. 1997; Hooper et al. 1997; Boyce et al. 1998, McLure et al. 1999; Schade et al. 2000) and 2) they are generally located in cluster environments (e.g. McLure & Dunlop 2000). Since cluster cores typically have sizes $r_c \sim 100$ kpc, we could hope to detect radiation emitted by the nucleus of a cluster cD galaxy up to a few times $r_c/c \sim 10^6$ years ago and scattered by the hot intracluster gas towards us. Up to $\sim 1\%$ of nuclear emission should be Thomson scattered by free electrons within the gas. Since AGN are sources of radiation from radio to gamma-rays, scattering should add to the surface brightness of the cluster gas at various wavelengths.

Previous theoretical efforts in this direction have focused on the prospects for detecting scattered strongly polarized AGN radiation at radio and optical wavelengths (Sunyaev 1982; Gilfanov et al. 1987a; Sholomitskii & Yaskovich 1990; Wise & Sarazin 1990, 1992; Sarazin & Wise 1993; Murphy & Chernoff 1993). However, it would be particularly interesting to observe the scattered X-ray component, because a significant part of the AGN X-ray emission likely originates in the innermost regions of the accretion flow, within a few gravitational radii from the central black hole. At the same time, the detection of these scattered X-rays appears a challenging task, because the intracluster gas is itself a powerful X-ray emitter.

One feasible way to detect the scattered X-rays against the thermal emission of the hot gas would be to perform observations at $E \gg kT$, where E is the photon energy and $kT \sim 1\text{--}10$ keV is the gas temperature. Indeed, the AGN spectrum is power-law, $F_{\text{AGN}} \propto E^{-\Gamma}$ with $\Gamma \sim 1$, while the plasma bremsstrahlung spectrum is exponentially declining, $F_{\text{gas}} \propto \exp(-E/kT)$, at $E \gg kT$. Unfortunately, the angular resolution and sensitivity of present-day hard X-ray telescopes are not sufficient for mapping clusters of galaxies and detecting scattered AGN radiation. However, the situation may improve dramatically with the advent of grazing incidence X-ray telescopes sensitive up to ~ 40 keV, such as those being under consideration for the projected Constellation-X (<http://constellation.gsfc.nasa.gov/docs/main.html>) and XEUS (http://astro.esa.int/SA-general/Projects/XEUS/main/xeus_main.html) missions. Furthermore, given the very large collecting area (several square meters) of these planned telescopes in the standard X-ray band, it should become possible to search for scattered X-rays from distant radio galaxies and quasars (at redshifts $z \gtrsim 1$). Indeed, since the radiation from the quasar gets redshifted on its way to us, a significant gain

in the ratio $F_{\text{AGN}}/F_{\text{gas}} \propto [E(1+z)]^{-\Gamma} \exp[E(1+z)/kT]$ could be achieved already at $E \sim 10$ keV. Such observations would permit to constrain the lifetime of quasars and the parameters of the hot gas around them. This possibility is one of the issues discussed in the present paper (particularly in §3.2).

On the observational side, evidence has been accumulated over the recent years that AGN are often surrounded by gas atmospheres typical of clusters of galaxies. Early ROSAT observations indicated the presence of luminous extended X-ray emission around several powerful quasars with redshifts out to $z = 0.73$ (Crawford et al. 1999; Hardcastle & Worrall 1999). More recently, the Chandra observatory clearly resolved extended hot gas around several relatively nearby AGN, including 3C295 ($z = 0.461$, Harris et al. 2000), 3C220.1 ($z = 0.62$, Worrall et al. 2001), 3C123 ($z = 0.2177$, Hardcastle et al., 2001), Cyg A ($z = 0.0562$, Smith et al. 2002), and H1821+643 ($z = 0.297$, Fang et al. 2002).

Chandra has also detected luminous extended (to radii ~ 100 kpc) X-ray emission surrounding two high-redshift powerful radio galaxies 3C294 at $z = 1.786$ (Fabian et al. 2001) and PKS 1138-262 at $z = 2.156$ (Carilly et al. 2002). Assuming for these objects that the emission of the central source is isotropic and its X-ray luminosity has been the same in the past as it is now (\sim a few 10^{45} erg s $^{-1}$), we are able to estimate (see §3.2) that the gas surface brightness should be dominated by scattered power-law radiation from the AGN already at $E \gtrsim 10$ keV.

In this paper we also discuss another possibility to detect scattered nuclear X-ray radiation. We show (in §2 and §3.3) that at least for nearby AGN located in clusters cD galaxies or in isolated giant elliptical galaxies, one can gain significantly by measuring the scattered surface brightness in resonance X-ray lines rather than in the continuum. Such observations would ideally require high (\sim a few eV) spectral resolution in order to separate the resonance lines from other lines. The needed resolution together with high sensitivity is to be achieved with projected high-energy astrophysics observatories such as Astro-E2, Constellation-X and XEUS. As an example, we estimate (in §4) the level of constraints that should be possible to derive on the past X-ray luminosity of the nearby M87 and Cyg A active galaxies.

2. Advantage of scattered X-ray lines over the scattered continuum

Consider an AGN surrounded by hot ($T \gtrsim 10^7$ K) gas. The following emission components will contribute to the X-ray surface brightness of the gas:

- First, there is X-ray emission (line plus continuum) of the hot plasma in which collisional ionization and excitation dominate. However, a bright AGN may additionally photoionize the plasma. In our calculations

below we fully neglect this effect, although it can be important when the AGN luminosity is very high (quasar-like), as will be discussed in a separate paper (Sazonov & Sunyaev, in preparation).

- Second, there is radiation emitted by the AGN and Thomson scattered by free electrons in the gas. This scattered radiation contributes to the surface brightness in the spectral continuum.
- Finally, AGN photons with energies falling within the cores of X-ray lines of ions of heavy elements can resonantly scatter on these ions, thus contributing to the surface brightness in the lines.

Consider an optically thin volume of gas with electron temperature T and number density N_e , exposed to an external spectral flux $F_E(E)$ (measured in units of $\text{erg cm}^{-2} \text{ s}^{-1} \text{ keV}^{-1}$).

The plasma continuum spectral emissivity due to bremsstrahlung is given by (e.g. Zombeck 1990)

$$\epsilon_{E,\text{cont}}(E) = 2.3 \times 10^{-20} T^{-1/2} \exp(-E/kT) N_e^2 g_B(T, E) \quad (\text{erg cm}^{-3} \text{ s}^{-1} \text{ keV}^{-1}), \quad (1)$$

where g_B is the corresponding Gaunt factor.

The energy-integrated emissivity in a resonance line by ions of type z due to electron collisional excitation of an electron from the ground level i to an excited level k is given as (e.g. Zombeck 1990)

$$\epsilon_{\text{line}} = 2.7 \times 10^{-15} T^{-1/2} \exp(-E_{ik}/kT) \times N_e N_z(T) f_{ik} g_{ik}(T) \quad (\text{erg cm}^{-3} \text{ s}^{-1}), \quad (2)$$

where N_z is the ion number density, which depends on the gas temperature. The remaining quantities appearing in equation (2), namely E_{ik} , f_{ik} and g_{ik} , characterize the line itself, denoting its energy, oscillator strength and excitation Gaunt factor, respectively.

The rate (per unit volume) of Thomson scattering of the external radiation, integrated over the scattering angle θ , is

$$\begin{aligned} \epsilon_{E,\text{cont}}^{\text{scat}}(E) &= \frac{3}{8} \int_{-1}^1 d \cos \theta (1 + \cos^2 \theta) \epsilon_{E,\theta,\text{cont}}^{\text{scat}}(E, \theta) \\ &= F_E(E) N_e \sigma_T \quad (\text{erg cm}^{-3} \text{ s}^{-1} \text{ keV}^{-1}) \end{aligned} \quad (3)$$

where $\sigma_T = 6.65 \times 10^{-25}$ is the Thomson scattering cross section. Note that we ignore throughout the Klein–Nishina correction to the scattering cross section as well the change in the photon frequency by scattering, which is justifiable if $E \ll mc^2$ and $kT \ll mc^2$, where $mc^2 = 511 \text{ keV}$ is the electron rest energy.

The energy-integrated rate of resonant scattering (integrated over the scattering angle) of the external radiation in the line $i \rightarrow k$ by ions z is

$$\begin{aligned} \epsilon_{\text{line}}^{\text{scat}} &= 4.1 \times 10^{-18} \pi \\ &\times F_E(E_{ik}) N_z(T) r_e c f_{ik} \quad (\text{erg cm}^{-3} \text{ s}^{-1}), \end{aligned} \quad (4)$$

where $r_e = 2.82 \times 10^{-13} \text{ cm}$ is the classical electron radius, c is the speed of light, and the numerical coefficient accounts for the unit transition from Hz to keV.

From equations (1) and (3) we can find the ratio of the Thomson scattering rate to the bremsstrahlung emissivity:

$$\begin{aligned} \frac{\epsilon_{E,\text{cont}}^{\text{scat}}}{\epsilon_{E,\text{cont}}}(E) &= 2.9 \times 10^{-5} \\ &\times F_E(E) T^{1/2} \exp(E/kT) N_e^{-1} g_B^{-1}(T, E). \end{aligned} \quad (5)$$

The ratio of the resonant scattering rate to the emissivity in the line $i \rightarrow k$ is given by a similar expression which follows from equations (2) and (4),

$$\begin{aligned} \frac{\epsilon_{\text{line}}^{\text{scat}}}{\epsilon_{\text{line}}} &= 4.1 \times 10^{-5} \\ &\times F_E(E_{ik}) T^{1/2} \exp(E_{ik}/kT) N_e^{-1} g_{ik}^{-1}(T). \end{aligned} \quad (6)$$

We can now compare the ratios (6) and (5) with each other for $E = E_{ik}$:

$$R \equiv \frac{\epsilon_{\text{line}}^{\text{scat}}}{\epsilon_{\text{line}}} / \frac{\epsilon_{E,\text{cont}}^{\text{scat}}}{\epsilon_{E,\text{cont}}} = 1.4 \frac{g_B(T, E_{ik})}{g_{ik}(T)}. \quad (7)$$

In the low-temperature limit ($kT \ll E_{ik}$), the excitation Gaunt factor g_{ik} ranges between 0.1 and 0.25 for most interesting lines; it slowly increases with temperature and becomes $g_{ik} = 0.2\text{--}0.3$ at $kT \sim E_{ik}$ (e.g. Mewe et al. 1985). The bremsstrahlung Gaunt factor also is a weak function of temperature: $g_B = (E/kT)^{-0.4}$ when $E \sim kT$. Summarizing these facts, we may simply write

$$R \sim 6 \text{ for } kT \sim E_{ik}. \quad (8)$$

This approximate relation is accurate to within a factor of 3 for all resonance X-ray lines of interest to us. Fig. 1 shows, for several resonance lines, the dependence $R(T)$ computed using the MEKAL plasma emission code in combination with other atomic data sources (see §4 for details). In these computations taken into account was the contribution to ϵ_{line} of unresolved (defined as those with energies within one Doppler width from the resonance energy) satellite lines. This effectively leads to a smaller value of R as compared to the definition (7). However, this reduction is only significant for the 6.70 keV and 6.97 keV $\text{K}\alpha$ lines or iron when $kT \ll E_{ik}$. We should note that the large values ($R \sim 20$ at $kT \sim E_{ik}$) obtained for the iron L-shell lines at 1.13 keV and 1.17 keV may be partly the result of the different values for the oscillation strengths being used in the MEKAL code with which we compute ϵ_{line} and in the list of resonance lines of Verner et al. (1996) which we use to compute $\epsilon_{\text{line}}^{\text{scat}}$. We do not attempt in this paper to correct for this and possibly other inconsistencies caused by the simultaneous use of several sources of atomic data. However, we estimate that some of our computational results obtained below (in §4), may contain a relative systematic error of $\lesssim 2$.

We point out that R is typically several times smaller for intercombination lines than for resonance lines and

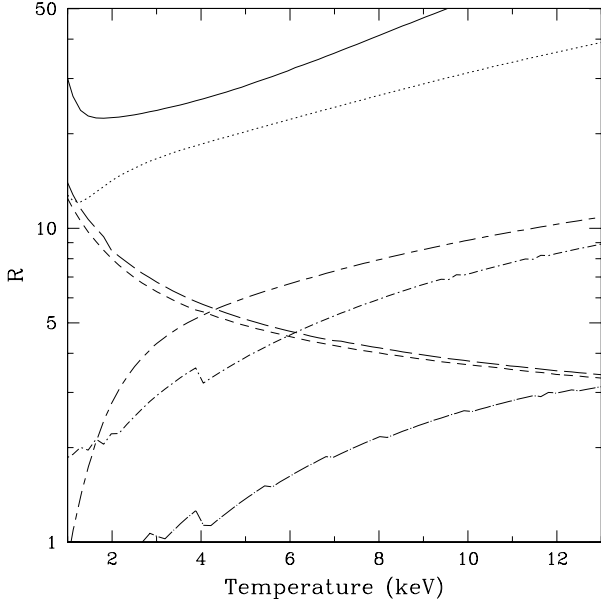


Fig. 1. The ratio R defined by eq. [7] as a function of plasma temperature for different resonance X-ray lines: Fe XXIII L-shell line at 1.13 keV (solid), Fe XXIV L-shell line at 1.17 keV (dotted), Si XIII K α line at 1.86 keV (short-dashed), S XV K α line at 2.46 keV (long-dashed), Fe XXV K α line at 6.70 keV (dot-short-dashed), Fe XXVI Ly α line at 6.97 keV (dot-long-dashed), and Fe XXV K β line at 7.88 keV (short-dash-long-dashed).

$R \approx 0$ for forbidden lines. For this reason we consider only resonance lines throughout.

We have thus found that for a given resonance line with energy E_{ik} , the relative contribution of scattered external radiation to the volume X-ray emissivity of hot gas is typically larger by a significant factor of the order of 3–10 than for the continuum at E_{ik} . We also know that for typical cluster temperatures $kT \sim$ a few keV the combined surface brightness of the intracluster gas in the resonance X-ray lines with $E_{ik} \sim kT$ is comparable to that in the continuum. We therefore arrive at the conclusion that resonance X-ray lines present significant advantage over the continuum for searches of scattered nuclear radiation in clusters of galaxies and elliptical galaxies performed at $E \sim kT$.

After we have introduced the R factor in equation (7) and shown that this factor is only weakly dependent on the resonance line and on gas temperature, we can continue our treatment in parallel for continuum and line emission.

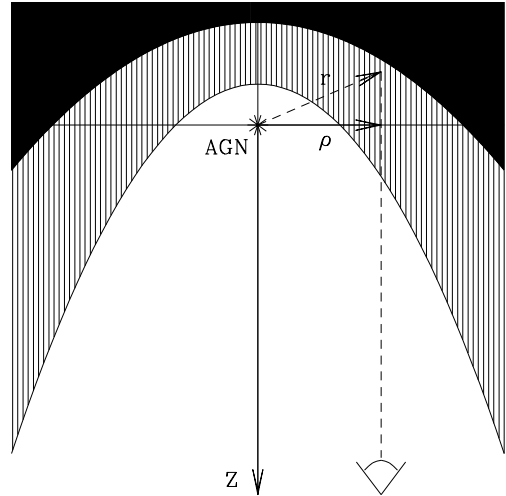


Fig. 2. A sketch of the flare and the switch-off scenario. The points with equal travel time from the AGN to the observer lie on a paraboloid. In the switch-off case, the thermal plasma located in the light-grey and grey regions is scattering the radiation emitted by the AGN. In the case of a flare of the AGN, only the light-grey area is filled by photons and contributing to the scattered emission. A possible path for a photon scattered into the line of sight of the observer is marked by a dashed line. The system is rotationally symmetric about the z-axis.

3. AGN in the center of a beta cluster

We shall now consider the following model (see Fig. 2). A supermassive black hole is located in the center of a cluster of galaxies containing hot gas with a beta-law radial density profile (Cavaliere & Fusco-Femiano 1976):

$$N_e = N_0 (1 + r^2/r_c^2)^{-3\beta/2}, \quad (9)$$

where N_0 is the central electron number density and r_c is the core-radius. The gas temperature T and element abundances are constant over the cluster.

At a moment $t_{\text{on}} = -\Delta$ (as measured by an earth bound observer) the central source switches on (i.e. becomes an AGN) and at a later moment $t_{\text{off}} = 0$ it switches off. The AGN emits isotropically X-ray radiation having a power-law spectrum of photon index α , at a constant luminosity L_X in the energy band $[E_1, E_2]$:

$$L_X = A \int_{E_1}^{E_2} E^{-\alpha} E \, dE = A \frac{E_2^{2-\alpha} - E_1^{2-\alpha}}{2 - \alpha}. \quad (10)$$

The spectral flux at a given distance r from the AGN is therefore

$$F_E = \frac{(2-\alpha)L_X}{4\pi(E_2^{2-\alpha} - E_1^{2-\alpha})r^2} E^{1-\alpha}. \quad (11)$$

Our goal is to find the surface brightness profile of the cluster, including the contribution of scattered AGN radiation, at a given moment of time $t > t_{\text{on}}$.

3.1. Approximation of isotropic scattering

We shall use throughout the approximation of isotropic scattering. This simplifies the treatment but requires explanation. We know that in reality Thomson scattering occurs according to the Rayleigh phase function $p(\cos\theta) = 3(1 + \cos^2\theta)/8$. In the case of resonant scattering, the phase function depends on the line and generally can be represented as a weighted sum of the Rayleigh phase function and the isotropic function $p(\cos\theta) = 1/2$ (see e.g. Chandrasekhar 1950). However, for our given geometry of the problem the resulting brightness profiles depend only weakly (typically by less than 10%) on the phase function. For this reason, the approximation of isotropic scattering is quite reasonable.

3.2. Continuum radiation

We shall first consider the X-ray spectral continuum, for which the relevant scattering mechanism is Thomson scattering on free electrons. Since the Thomson optical depths of the hot atmospheres of clusters of galaxies and elliptical galaxies are small, $\tau_T \lesssim 0.01$, we can use the single-scattering approximation and make some analytic estimates.

The continuum (bremsstrahlung) surface brightness of a beta cluster is described, as a function of projected distance ρ from the nucleus, by the well-known formula, which can be obtained by integrating the plasma emission along a given line of sight (i.e. along the coordinate z – see Fig. 2) using equations (1) and (9):

$$\begin{aligned} B_{E,\text{cont}} &\equiv \int_{-\infty}^{\infty} \frac{\epsilon_{E,\text{cont}}(r)}{4\pi} dz \\ &= 2.9 \times 10^{-5} \frac{\Gamma(3\beta - 1/2)}{\Gamma(3\beta)} \left(\frac{N_0}{0.01 \text{ cm}^{-3}} \right)^2 \frac{r_c}{100 \text{ kpc}} \\ &\times \left(\frac{kT}{1 \text{ keV}} \right)^{-1/2} (E/kT)^{-0.4} \exp(-E/kT) \\ &\times (1 + \rho^2/r_c^2)^{-3\beta+1/2} \\ &\text{(erg cm}^{-2} \text{ s}^{-1} \text{ sr}^{-1} \text{ keV}^{-1}), \end{aligned} \quad (12)$$

where $r = (\rho^2 + z^2)^{1/2}$ and we have assumed $g_B(T, E) = (E/kT)^{-0.4}$.

The surface brightness of the Thomson scattered radiation from the AGN is given by

$$B_{E,\text{cont}}^{\text{scat}} \equiv \int_{z_1}^{z_2} \frac{\epsilon_{E,\text{cont}}^{\text{scat}}(r)}{4\pi} dz = \frac{\sigma_T}{4\pi} \int_{z_1}^{z_2} F_E(r) N_e(r) dz, \quad (13)$$

where we have used equation (3) and our assumption of isotropic scattering.

The time-dependent integration limits $z_1(t, \rho)$ and $z_2(t, \rho)$ in equation (13) are determined by the loci of scattering sites giving a fixed time delay \tilde{t} . If the distance between the emitter and the observer is much larger than the characteristic size of the scattering cloud, which is true in our case, the constant-delay surface is a paraboloid with the focus at the position of the source (see e.g. Sunyaev & Churazov 1998 and references therein to earlier work considering similar light-echo problems):

$$z(\tilde{t}, \rho) = \frac{1}{2} \left(\frac{\rho^2}{c\tilde{t}} - ct \right). \quad (14)$$

Therefore,

$$z_1(t, \rho) = \frac{1}{2} \left[\frac{\rho^2}{c(t + \Delta)} - c(t + \Delta) \right], \quad (15)$$

$$z_2(t, \rho) = \begin{cases} (\rho^2/ct - ct)/2 & \text{if } 0 < t \\ \infty & \text{if } -\Delta < t < 0. \end{cases} \quad (16)$$

The integration limits in equation (13) depend for given t and ρ on the outburst duration Δ . We shall first consider two limiting cases for which analytic treatment is possible.

3.2.1. Stationary case

Let the AGN be a persistent source. The limits for the integral $\int_{z_1}^{z_2} \epsilon_{E,\text{cont}}^{\text{scat}} dz$ are then $z_1(t, \rho) = -\infty$ and $z_2(t, \rho) = \infty$, and it is possible, using equation (9) for $N_e(r)$ and equation (11) for F_E , to express the integral through hypergeometric functions. In the particular interesting case of $\beta = 2/3$, the scattered surface brightness is

$$\begin{aligned} B_{E,\text{cont}}^{\text{scat}}(\beta = 2/3) &= 6.0 \times 10^{-5} \frac{L_X}{L_{\text{Edd}}} \frac{M_{\text{BH}}}{10^9 M_{\odot}} \frac{N_0}{0.01 \text{ cm}^{-3}} \\ &\times \frac{100 \text{ kpc}}{r_c} \frac{2-\alpha}{10^{2-\alpha}-1} \left[r_c/\rho - (1 + \rho^2/r_c^2)^{-1/2} \right] E^{1-\alpha} \\ &\text{(erg cm}^{-2} \text{ s}^{-1} \text{ sr}^{-1} \text{ keV}^{-1}), \end{aligned} \quad (17)$$

where M_{BH} is the mass of the central black hole, $L_{\text{Edd}} = 1.4 \times 10^{38} M_{\text{BH}}/M_{\odot}$ is the corresponding Eddington luminosity, L_X is the AGN luminosity in the energy range 1-10 keV, and E is measured in keV.

The ratio of the scattered surface brightness to the intrinsic surface brightness of the gas in the X-ray continuum is

$$\begin{aligned} \frac{B_{E,\text{cont}}^{\text{scat}}}{B_{E,\text{cont}}}(\beta = 2/3) &= 2.3 \frac{L_X}{L_{\text{Edd}}} \frac{M_{\text{BH}}}{10^9 M_{\odot}} \frac{0.01 \text{ cm}^{-3}}{N_0} \\ &\times \left(\frac{100 \text{ kpc}}{r_c} \right)^2 \left(\frac{kT}{1 \text{ keV}} \right)^{0.1} \frac{2-\alpha}{10^{2-\alpha}-1} \\ &\times (1 + \rho^2/r_c^2)^{3/2} \left[r_c/\rho - (1 + \rho^2/r_c^2)^{-1/2} \right] \\ &\times E^{1.4-\alpha} \exp(E/kT). \end{aligned} \quad (18)$$

We can also write down asymptotic expressions applicable in the limit of $\rho \gg r_c$ for arbitrary values of β :

$$B_{E,\text{cont}}^{\text{scat}}(\rho \gg r_c) = 3.2 \times 10^{-5} \frac{\Gamma(3\beta/2 + 1/2)}{\Gamma(3\beta/2 + 1)} \frac{L_X}{L_{\text{Edd}}} \frac{M_{\text{BH}}}{10^9 M_{\odot}} \times \frac{N_0}{0.01 \text{ cm}^{-3}} \frac{100 \text{ kpc}}{r_c} \frac{2 - \alpha}{10^{2-\alpha} - 1} (\rho/r_c)^{-3\beta-1} E^{\alpha-1} (\text{erg cm}^{-2} \text{ s}^{-1} \text{ sr}^{-1} \text{ keV}^{-1}); \quad (19)$$

$$\begin{aligned} B_{E,\text{cont}}^{\text{scat}}(\rho \gg r_c) &= 1.1 \frac{\Gamma(3\beta/2 + 1/2)\Gamma(3\beta)}{\Gamma(3\beta/2 + 1)\Gamma(3\beta - 1/2)} \frac{L_X}{L_{\text{Edd}}} \\ &\times \frac{M_{\text{BH}}}{10^9 M_{\odot}} \frac{0.01 \text{ cm}^{-3}}{N_0} \left(\frac{100 \text{ kpc}}{r_c} \right)^2 \left(\frac{kT}{1 \text{ keV}} \right)^{0.1} \\ &\times \frac{2 - \alpha}{10^{2-\alpha} - 1} (\rho/r_c)^{3\beta-2} E^{1.4-\alpha} \exp(E/kT). \end{aligned} \quad (20)$$

It can also be shown that within the cluster core, $B_{E,\text{cont}}^{\text{scat}} \propto \rho^{-1}$ and $B_{E,\text{cont}}^{\text{scat}}/B_{E,\text{cont}} \propto \rho^{-1}$ for any β , i.e. the contribution of scattered radiation increases with approaching the AGN. This can be directly verified for $\beta = 2/3$ using equation (18).

Fig. 3 demonstrates the dependence of the surface brightness profile of a model cluster with a central AGN on the β parameter. The scattered surface brightness profiles were derived by numerical integration of equation (13). Fig. 4 shows the corresponding plots for the ratio of the scattered surface brightness to the intrinsic surface brightness of the intracluster gas. We see both from Fig. 4 and equation (20) that outside the core region (at $\rho \gtrsim r_c$), the relative contribution of scattered AGN radiation to the surface brightness diminishes with increasing ρ when $\beta < 2/3$; it increases with distance when $\beta > 2/3$.

The example with $\beta = 1/3$ presented in Figs. 3 and 4 illustrates a situation that resembles cluster cooling flows. Typically, gas density grows $\propto r^{-1}$ towards the center of the cooling flow, which roughly corresponds to a beta model with a small r_c , large N_0 and $\beta \approx 1/3$. We then find from equations (12) and (19) that $B_{E,\text{cont}} \propto \rho^{-1}$ and $B_{E,\text{cont}}^{\text{scat}} \propto \rho^{-2}$ (assuming a constant temperature) for cooling flows. Interestingly, the surface brightness profile of scattered AGN radiation within the core of a beta cluster (see above) is similar ($\propto \rho^{-1}$) to the intrinsic brightness profile of an (isothermal) cooling flow. Of course, a cluster core dominated by scattered emission from a central powerful quasar will have a very different spectrum (power law) than a standard cooling flow.

The factor $E^{1.4-\alpha} \exp(E/kT)$ appearing in equations (18) and (20) represents the dependence on photon energy. It has a minimum (for $\alpha > 1.4$) at $E = (\alpha - 1.4)kT$ and increases exponentially with energy when $E \gg kT$. The origin of this dependence is obvious: we are comparing the slowly declining (power-law) spectrum of the AGN emission with the exponentially decaying efficiency of collisional radiative mechanisms operating in the intracluster gas. It is clear that for given AGN luminosity and parameters of the gas, a significant gain (in terms of the relative

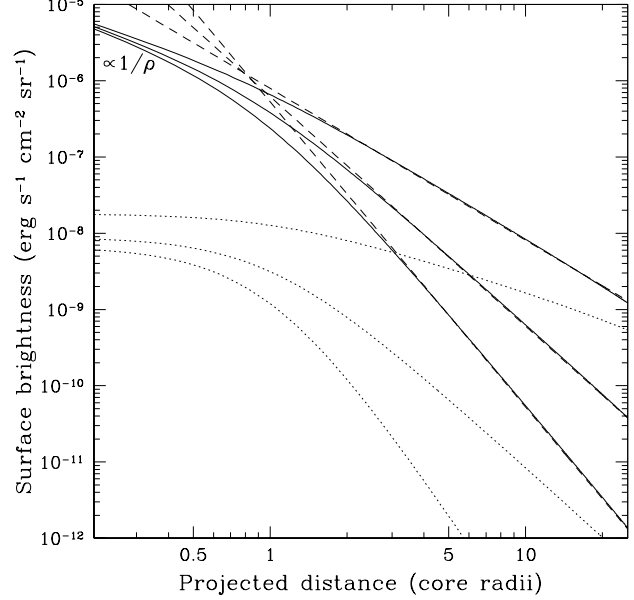


Fig. 3. Surface brightness profiles of scattered AGN radiation (solid lines) and plasma thermal emission (dotted lines) in the hard X-ray continuum at photon energy $E = 20$ keV, corresponding to a model in which the central black hole has a mass of $10^9 M_{\odot}$ and is a persistent X-ray source with $L_X = L_{\text{Edd}}$ and $\alpha = 2$. The host beta cluster has the following parameters: $r_c = 100$ kpc, $N_0 = 0.01 \text{ cm}^{-3}$, $kT = 3$ keV, and (from top to bottom) $\beta = 1/3, 2/3$ and 1. The object is local ($z \ll 1$). The dashed curves are $\rho \gg r_c$ asymptotes, given by eq. [19], for the scattered surface brightness; it can be seen that these asymptotes are applicable at $\rho \gtrsim 2r_c$. In the opposite limit of $\rho \ll 1$ the scattered surface brightness is inversely proportional to ρ and is independent of β , as indicated in the upper left corner of the figure.

contribution of scattered AGN radiation to the surface brightness) can be achieved by performing observations at high energies $E \gg kT$, like in our examples in Figs. 3 and 4. A cautionary note is necessary here. If one wants to constrain the past AGN luminosity by measuring the hard X-ray surface brightness of a cluster dominant galaxy or of a giant elliptical galaxy, a restriction will appear due to a significant contribution to the measured surface brightness from the (unresolved) X-ray binaries of the galaxy. We estimate that in practice it should be very difficult to obtain limits better than $L_X \gtrsim 10^{-3} L_{\text{Edd}}$. Of course, this complication is irrelevant for surface brightness measurements carried out over regions of a galaxy cluster that are devoid of point X-ray sources, say at distances ~ 100 kpc from the nucleus of a central dominant galaxy.

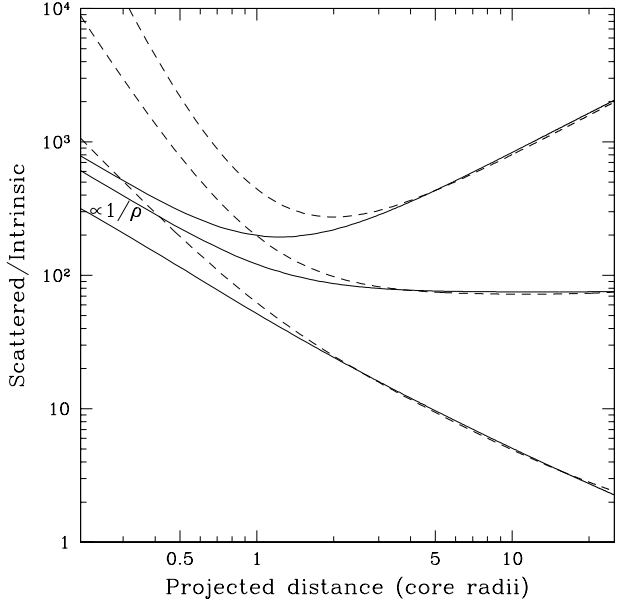


Fig. 4. Radial profiles of the ratio of the surface brightness of scattered AGN radiation to the intrinsic brightness of the beta-cluster gas, for the same model as in Fig. 3. The solid curves correspond (from top to bottom) to $\beta = 1/3, 2/3$ and 1 . The dashed curves are the corresponding $\rho \gg r_c$ asymptotes given by eq. [20].

3.2.2. The case of a high-redshift AGN

Furthermore, if a powerful quasar or a radio galaxy is observed at high redshift z , the relevant factor will be $[E(1+z)]^{1.4-\alpha} \exp[E(1+z)/kT]$. Consider for example the radio galaxy 3C294 located at $z = 1.786$, for which recent Chandra X-ray observations (Fabian et al. 2002) clearly revealed the presence of a surrounding intracluster medium. Since the total number of counts registered from the source in the 20 ksec Chandra observation is small, ~ 100 , of which only ~ 30 are from the central AGN, it is only possible to make rough estimates in this case. Fabian et al. find that the gas temperature is ~ 5 keV, the 2-10 keV rest-frame luminosity of the hot gas is $\sim 2.5 \times 10^{44}$ erg s $^{-1}$, the 2-10 keV rest-frame (isotropic) luminosity of the central AGN is $\sim 1.1 \times 10^{45}$ erg s $^{-1}$, the photon index for the AGN emission $\alpha \sim 2$ and the radial Thomson depth of the cluster is ~ 0.004 .

We can then estimate that the ratio of the flux of scattered nuclear radiation to that of thermal bremsstrahlung emission from the gas is only $\sim 1\%$ at $E \lesssim 2$ keV, $\sim 3\%$ at $E = 3$ keV, $\sim 30\%$ at $E = 10$ keV, ~ 1 at $E = 12$ keV and ~ 4 at $E = 15$ keV. We stress that these estimates assume that the central source is isotropic, that its luminosity has been the same in the recent past (over \sim

few 10^5 years) as it is now, and are made for the total flux from the entire observed X-ray halo (of ~ 15 arcsec, or equivalently ~ 100 kpc radius). We thus see that it is desirable to go to energies $E > 10$ keV in order to search for scattered nuclear radiation around the 3C294 galaxy. Of course, photon statistics then becomes a limiting factor for observations of such a distant object. We can roughly estimate that the XEUS observatory with its effective area of ~ 2 m 2 at 10 keV and angular resolution of a few arcsec should be able to detect a total of a few tens of scattered AGN photons above 10 keV in a 100 ks observation of 3C294. This, combined with much more accurate measurements of the surface brightness of the intracluster gas in the standard X-ray band, could be only about enough to put constraints on the past history of the 3C294 central X-ray luminosity.

Another similar example is the radio galaxy PKS 1138–262 at $z = 2.2$, from which Chandra also has observed luminous extended X-ray emission (Carilly et al. 2002). In this case, the X-ray luminosity of the gas is similar to that of the 3C294 cluster (unfortunately, the gas temperature is unconstrained), but the inferred 2-10 keV (rest-frame) luminosity of the central source is four times higher, $\sim 4 \times 10^{45}$ erg s $^{-1}$. It may therefore be possible to detect several times more scattered photons with energies above 10 keV in XEUS observations of this object compared to the case of 3C294. Moreover, it is likely that in this case the gas emission will be dominated by scattered radiation from the AGN already at $E \gtrsim 5$ keV (due to the higher redshift and luminosity), so that at least several hundreds of scattered AGN photons above 5 keV could be detected in a 100 ks XEUS-2 observation of PKS 1138–262 (taking into account the larger collecting area of the telescope at the lower energies).

We note that photon statistics should be less of a problem for more nearby AGN and quasars such as 3C 273 located at $z = 0.158$. In fact, it is quite possible, given the huge X-ray luminosity of the 3C 273 quasar, $\sim 2 \times 10^{46}$ erg s $^{-1}$ (e.g. Yaqoob & Serlemitsos 2000), that a hot intracluster medium surrounding it, if any, will be first revealed in scattered X-rays from the central source rather than by its own emission.

3.2.3. Short AGN flare

Consider now a situation in which there was a short AGN outburst in the past, between $t_{\text{on}} = -\Delta$ and $t_{\text{off}} = 0$ (and the observation is taking place at $t > 0$). The “short” here means that the line-of-sight depth of the illuminated (light-grey in Fig. 2) zone of the cluster must be much smaller than the characteristic size at a given projection radius. Therefore one of the following conditions must be fulfilled: $\Delta \ll r_c/c$ if $\rho \lesssim r_c$ or $\Delta \ll \rho/c$ if $\rho \gtrsim r_c$. Then, as follows from equations (15) and (16),

$$\delta z(t, \rho) \equiv z_2 - z_1 \approx \frac{c\Delta}{2}(1 + \rho^2/c^2 t^2), \quad (21)$$

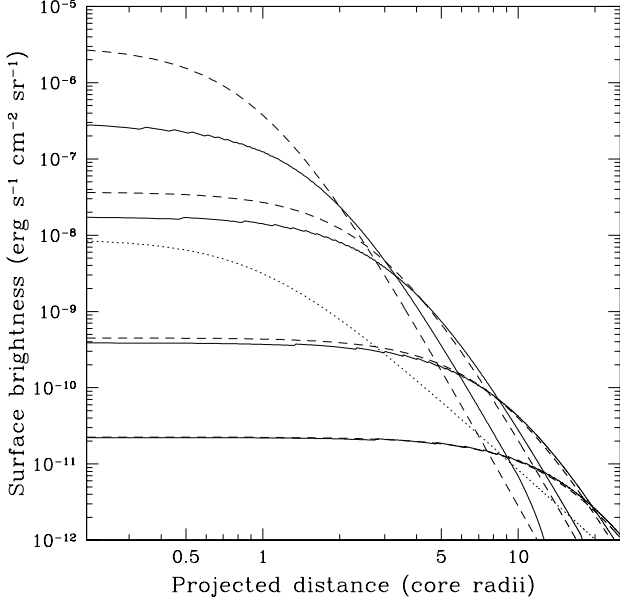


Fig. 5. Surface brightness profiles of scattered AGN radiation (solid lines) in the hard X-ray continuum at $E = 20$ keV, measured at different times ($t = r_c/c, 3r_c/c, 9r_c/c$ and $19r_c/c$) after a short ($\Delta = r_c/c$) flare with $L_X = L_{\text{Edd}}$ and $\alpha = 2$ of the central black hole of $10^9 M_\odot$ mass. The gas parameters are $r_c = 100$ kpc, $N_0 = 0.01 \text{ cm}^{-3}$, $kT = 3$ keV, and $\beta = 2/3$. The dashed curves are $\rho, ct \gg r_c$ asymptotes given by eq. [22]. The dotted line is the surface brightness profile of plasma thermal emission.

and $\int_{z_1}^{z_2} \epsilon_{E,\text{cont}}^{\text{scat}}(\rho, z) dz \approx \epsilon_{E,\text{cont}}^{\text{scat}}(\rho, z_2) \delta z(\rho)$. We then find in the limit of $\rho, ct \gg r_c$

$$\begin{aligned} B_{E,\text{cont}}^{\text{scat}} &= 3.2 \times 10^{-5} \times 4^{3\beta/2} \frac{L_X}{L_{\text{Edd}}} \frac{M_{\text{BH}}}{10^9 M_\odot} \\ &\times \frac{N_0}{0.01 \text{ cm}^{-3}} \frac{100 \text{ kpc}}{r_c} \frac{2 - \alpha}{10^{2-\alpha} - 1} \\ &\times (\Delta/t)(r_c/ct)^{3\beta+1} (1 + \rho^2/c^2 t^2)^{-3\beta-1} E^{1-\alpha} \\ &(\text{erg cm}^{-2} \text{ s}^{-1} \text{ sr}^{-1} \text{ keV}^{-1}); \end{aligned} \quad (22)$$

$$\begin{aligned} \frac{B_{E,\text{cont}}^{\text{scat}}}{B_{E,\text{cont}}} &= 1.2 \times 4^{3\beta/2} \frac{\Gamma(3\beta)}{\Gamma(3\beta - 1/2)} \frac{L_X}{L_{\text{Edd}}} \frac{M_{\text{BH}}}{10^9 M_\odot} \\ &\times \frac{0.01 \text{ cm}^{-3}}{N_0} \left(\frac{100 \text{ kpc}}{r_c} \right)^2 \left(\frac{kT}{1 \text{ keV}} \right)^{0.1} \frac{2 - \alpha}{10^{2-\alpha} - 1} \\ &\times (\Delta/t)(ct/r_c)^{3\beta-2} (\rho/ct)^{6\beta-1} (1 + \rho^2/c^2 t^2)^{-3\beta-1} \\ &\times E^{1.4-\alpha} \exp(E/kT). \end{aligned} \quad (23)$$

Comparing equations (23) and (20), we see that for a given luminosity L_X the contribution of scattered nuclear radiation to the surface brightness at $\rho \sim ct$ is smaller

by a factor of Δ/t in the flare case compared to the stationary case. This is expected, because in the former case the scattered radiation comes from a gas layer of width $\delta z \sim c\Delta$ along the line of sight, whereas $\delta z \sim \rho \sim ct$ in the latter case.

Fig. 5 shows an example of a sequence of scattered surface brightness profiles that would be measured at different times after a short AGN outburst. We see that distant regions of the cluster reveal no scattered light early on after the flare but become progressively brighter as time goes by and photons which were emitted by the AGN during the flare propagate through the gas. The ratio $B_{E,\text{cont}}^{\text{scat}}/B_{E,\text{cont}}$ has a maximum at $\rho_{\text{max}} \sim ct$, as indicated by equation (23). For example, $\rho_{\text{max}} = r_c$ when $\beta = 2/3$. Therefore, the zone of largest contribution of scattered AGN radiation propagates outwards with an apparent velocity equal to the speed of light. It is important for observations that this zone is broad — its effective radial extent $\delta\rho \sim \rho_{\text{max}} \sim ct$.

We also notice that the amplitude of the effect is proportional to the product $L_X \Delta$, i.e. to the total energy emitted by the AGN during the flare. Thus, for example, a 10^5 -year outburst at $L_X = 0.01 L_{\text{Edd}}$ would produce the same scattered surface brightness profile (at $\rho, ct \gg r_c$) as a 10^4 -year flare at $L_X = 0.1 L_{\text{Edd}}$.

3.2.4. Switch-off and switch-on scenarios

We can next consider a scenario in which the central source was persistently (over a time interval that is longer than the characteristic light travel time of the cluster) bright in the past until it suddenly turned off. An example of a sequence of scattered surface brightness profiles that would be measured at different times after the switch-off ($t > 0$) is shown in Fig. 6. One can see that the profiles differ markedly from those corresponding to the flare case (see Fig. 5). In particular, as time goes by the surface brightness decreases in the central region, while it remains practically unchanged in more distant parts of the cluster still for a long time $\sim \rho/c$ after the switch-off. This gives rise to a broad ($\delta\rho \sim \rho$) maximum of the scattered/intrinsic brightness ratio, which propagates outwards at an apparent speed of light.

Another interesting situation takes place when the central source is luminous at the time of observation but it turned on only recently. This “switch-on” case may actually correspond to the observed bright quasars, which may have been luminous for a time short compared to the light travel time of the gas around them. This situation is depicted in Fig. 7. One can see that the radial distribution of scattered AGN radiation is effectively truncated at a certain radius $\sim c(t - t_{\text{on}})$. This gives the possibility to estimate the time during which a quasar has been active by observing the scattered hard X-ray emission around it.

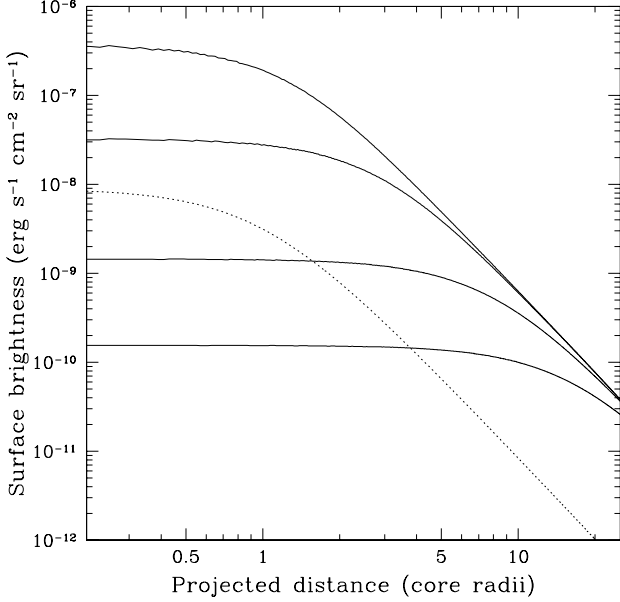


Fig. 6. Surface brightness profiles of scattered AGN radiation (solid lines) in the hard X-ray continuum at $E = 20$ keV, measured at different times ($t = r_c/c, 3r_c/c, 9r_c/c$ and $19r_c/c$ – the corresponding curves order from the uppermost to the lowermost) after the switch-off of the central source which emitted at $L_X = L_{\text{Edd}}$ with $\alpha = 2$ until time $t_{\text{off}} = 0$. Other parameters are the same as in Fig. 5. The dotted line shows the radial profile of plasma thermal emission.

3.3. Resonance lines

The results obtained above for the X-ray continuum can be straightforwardly generalized for the case of resonance lines provided the intracluster gas is optically thin ($\tau \ll 1$) to resonant scattering. We shall consider this limit below and then (in §3.3.1) point out differences that may arise in a situation when the gas has a significant optical depth ($\tau \gtrsim 1$) in a resonance line.

It is natural to present the results in terms of the equivalent line width. In the absence of external illumination, the equivalent width of a given line would be

$$\begin{aligned} EW_0 &= \int_{-\infty}^{\infty} \epsilon_{\text{line}} dz / \int_{-\infty}^{\infty} \epsilon_{E,\text{cont}}(E_{ik}) dz \\ &= 1.2 \times 10^5 \frac{N_z(T)}{N_e} f_{ik} \frac{g_{ik}(T)}{g_B(T, E_{ik})} \text{ (keV)}, \end{aligned} \quad (24)$$

under our assumptions of constant temperature and element abundances.

Resonant scattering in the hot gas of the AGN photons leads to an increase of the equivalent line width. At the same time, Thomson scattering of AGN radiation tends to

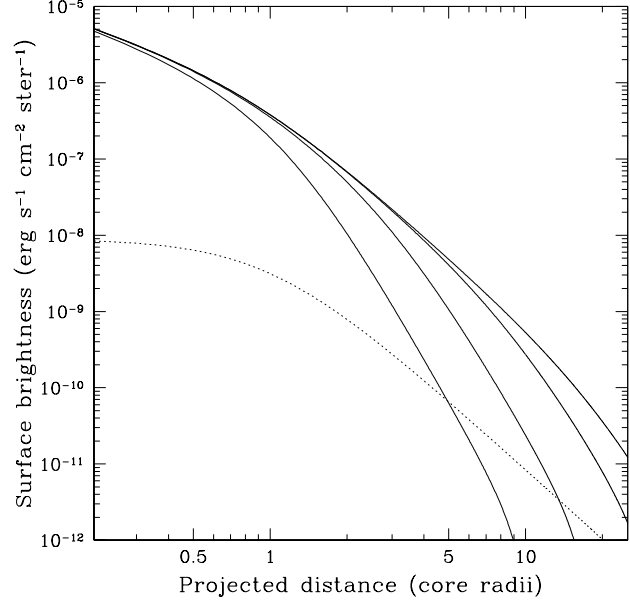


Fig. 7. Surface brightness profiles of scattered AGN radiation (solid lines) in the hard X-ray continuum at $E = 20$ keV, measured at different times ($t - t_{\text{ton}} = r_c/c, 3r_c/c, 9r_c/c$ and $19r_c/c$ – the corresponding curves order from the lowermost to the uppermost) after the switch-on of the central AGN with $L_X = L_{\text{Edd}}$ and $\alpha = 2$. Other parameters are the same as in Fig. 5. The dotted line shows the radial profile of plasma thermal emission.

enhance the continuum near the line and thus to decrease its equivalent width. As we know from §2, the first effect is a factor of $R \sim 6$ larger than the second, hence the net effect of the scattering of AGN emission in the intracluster gas should be the increased equivalent widths of the resonance lines. We can then write:

$$\begin{aligned} EW &= \left(\int_{-\infty}^{\infty} \epsilon_{\text{line}} dz + \int_{z_1}^{z_2} \epsilon_{\text{line}}^{\text{scat}} dz \right) / \\ &\quad \left(\int_{-\infty}^{\infty} \epsilon_{E,\text{cont}} dz + \int_{z_1}^{z_2} \epsilon_{E,\text{cont}}^{\text{scat}} dz \right) \\ &= EW_0 \frac{1 + R \int_{z_1}^{z_2} \epsilon_{E,\text{cont}}^{\text{scat}} dz / \int_{-\infty}^{\infty} \epsilon_{E,\text{cont}} dz}{1 + \int_{z_1}^{z_2} \epsilon_{E,\text{cont}}^{\text{scat}} dz / \int_{-\infty}^{\infty} \epsilon_{E,\text{cont}} dz}. \end{aligned} \quad (25)$$

If we assume that the contribution of scattered AGN radiation to the surface brightness of the cluster is small, then the fractional increase of the equivalent line width will be

$$\begin{aligned} \frac{\Delta EW}{EW_0} &\equiv \frac{EW - EW_0}{EW_0} \approx \\ &= (R - 1) \frac{\int_{z_1}^{z_2} \epsilon_{E,\text{cont}}^{\text{scat}}(E_{ik}) dz}{\int_{-\infty}^{\infty} \epsilon_{E,\text{cont}}(E_{ik}) dz}, \end{aligned} \quad (26)$$

with $R \sim 6$.

With the help of equation (26), one can readily apply all the results obtained in §3.2 to optically thin resonance lines.

It should be stressed that equation (26) is strictly valid only in the case where both the plasma temperature (which affects the ionization balance and plasma emissivity) and the element abundances are constant along the line of sight corresponding to a given projected distance ρ . Indeed, only when these conditions are met, $\epsilon_{\text{line}}(r) \propto \epsilon_{\text{cont}}(r)$ and $\epsilon_{\text{line}}^{\text{scat}}(r) \propto \epsilon_{\text{cont}}^{\text{scat}}(r)$ – see equations (1)–(4). In the general case, a coefficient different than $R - 1$ will relate the ratios $\Delta EW/EW_0$ and $\int_{z_1}^{z_2} \epsilon_{E,\text{cont}}^{\text{scat}} dz / \int_{-\infty}^{\infty} \epsilon_{E,\text{cont}} dz$.

We should also remind the reader that in the approximation we use throughout the paper, the radiation flux from the AGN does not influence the ionization balance (N_z) in the intracluster medium. The irradiation of the gas by a very bright central source will first of all alter the equivalent width of the emission line relative to the value predicted by equation (24); it will also affect (however to a smaller degree, because both ϵ_{line} and $\epsilon_{\text{line}}^{\text{scat}}$ are proportional to N_z) the ratio $\Delta EW/EW_0$.

3.3.1. Finite depth effects

The intracluster gas may be moderately optically thick to resonant scattering in the stronger X-ray lines ($\tau \gtrsim 1$, e.g. Gilfanov et al. 1987b), so the analytic results obtained above will be only approximately valid in such a case.

The optical depth at the center of a resonance line along a given direction \mathbf{l} through the cluster is given by the integral

$$\tau_0 = \int \sigma_0 N_z(r) dl. \quad (27)$$

At plasma temperatures typical of galaxy clusters ($kT \sim 1\text{--}10$ keV), all interesting X-ray lines have nearly Doppler absorption profiles whose width is determined by the velocities of thermal and turbulent motions, because the line natural width is relatively small. Therefore, the cross section at line center is

$$\sigma_0 = \frac{\sqrt{\pi} h r_e c f_{ik}}{\Delta E_D} \quad (28)$$

(h is Planck's constant), with the Doppler width being given by

$$\begin{aligned} \Delta E_D &= E_{ik} \left(\frac{2kT}{Am_p c^2} + \frac{V_{\text{turb}}^2}{c^2} \right)^{1/2} \\ &= E_{ik} \left[\frac{2kT}{Am_p c^2} (1 + 1.4AM^2) \right]^{1/2}, \end{aligned} \quad (29)$$

where A is the element atomic mass, m_p is the proton mass, and V_{turb} is the characteristic turbulent velocity.

The role of the additional line broadening caused by turbulence becomes more important with increasing atomic mass. This dependence is apparent from the second line of equation (29), which is expressed in terms of the turbulence Mach number M .

Taking into account the line broadening due to turbulent motions is important for two reasons. First, this effect may cause some resonance lines, which would otherwise be moderately optically thick, to become optically thin. Secondly, some satellite lines may fall within the core of the resonance line, thereby effectively reducing the factor R defined in equation (7). As was already noted in §2, this effect is particularly important for the $\text{K}\alpha$ lines of H-like and He-like iron at low temperatures $kT \sim 1$ keV.

When τ_0 becomes non-negligible, first of all the intrinsic surface brightness profile of the intracluster gas will be distorted due to diffusion of photons from the central region to the outer parts of the cluster. The equivalent line width will be somewhat smaller than predicted by equation (24) at $\rho \lesssim r_c$, and larger at $\rho \gtrsim r_c$ (Gilfanov et al. 1987b). Note that this effect takes place already at $\tau_0 < 1$, when only single resonant scatterings are important, and becomes more pronounced when $\tau_0 > 1$.

When the optical depth becomes larger than unity, multiple resonant scatterings will come into play. In the stationary scenario, the surface brightness profile of scattered AGN emission in a line with $\tau_0 \gtrsim 1$ will be flatter in the cluster core compared to a $1/\rho$ profile that would result in the case of $\tau_0 \ll 1$. Also, the total flux of AGN photons scattered towards us from the core region will be smaller than calculated in the single-scattering approximation by a factor $\sim \tau_0$. However, due to the rather similar effects taking place for thermal gas emission (see above), the net correction to the ratio W/W_0 (calculated in the limit $\tau_0 \ll 1$) is expected to be fairly small for $\tau_0 \gtrsim 1$.

Multiple resonant scatterings also delay the escape of AGN photons from the cluster core. As a result, the time-dependent scattered surface brightness profiles arising in the outburst scenario will be affected.

4. Numerical simulations

As a next step, we have performed numerical simulations for two actual clusters. These computations were based on a combination of 1) a Monte-Carlo code to play the diffusion of photons (both those emitted by the AGN and by the gas) through multiple resonant scatterings and 2) the MEKAL code (Mewe et al. 1986; Kaastra 1992; Liedahl et al. 1995) as implemented in the software package XSPEC v10 (Arnaud 1996) to calculate plasma emissivity in lines. The line energies and oscillator strengths were taken from the list of strong resonance lines of Verner, Verner & Ferland (1996). The solar abundances of elements were taken from Anders & Grevesse (1989). The ionization fractions were calculated using collisional ionization rate fits from Voronov (1997), radiative recombination rates from

Verner & Ferland (1996) and dielectronic recombination rates from Aldrovandi & Pequignot (1997), Shull & van Steenberg (1982) and Arnaud & Rothenflug (1985).

4.1. M87/Virgo

Apparently one of the most promising targets in the sky for observations of the discussed effect is M87. This is a giant elliptical galaxy located near the center of the nearest (17 Mpc – 1 arcmin corresponds to 5 kpc) rich cluster of galaxies Virgo. M87 hosts a central black hole of mass $3 \times 10^9 M_\odot$ (Macchetto et al. 1997; Marconi et al. 1997), which is the largest reliably measured black hole mass. The corresponding Eddington luminosity $L_{\text{Edd}} = 4 \times 10^{47}$ erg/s.

M87 demonstrates nuclear activity. In particular, observations at different energy bands reveal an unresolved nucleus and a one-sided jet. The combined bolometric luminosity of the nucleus and jet is of order 10^{42} erg s $^{-1}$, or $\sim 10^{-6}$ of the Eddington luminosity. This is an amazingly small value given the fact that the nucleus is located in the center of a dense cooling flow. The average power input in the form of relativistic plasma from the jet into a large-scale radio halo around M87 is estimated (Owen et al. 2000) to have been of order 10^{44} erg s $^{-1}$ over the past $\sim 10^8$ years, which is still a small fraction of the Eddington luminosity.

Both the nucleus and the jet (whose brightest knot is at a distance of ~ 1 kpc from the nucleus) have recently been observed in X-rays with the XMM-Newton (Boehringer et al. 2001) and Chandra (Wilson & Yang 2002) satellites. The X-ray spectrum is power-law with values for the photon index ranging between 2 and 2.9 for the nucleus and different knots in the jet. The inferred isotropic X-ray (1-10 keV) luminosities of the nucleus and the jet are $\sim 3 \times 10^{40}$ and 8×10^{40} erg, respectively (Boehringer et al. 2001).

In our simulations, we modeled the distribution of intracluster gas around M87 based on the results of recent analyses of the XMM observations by Boehringer et al. (2001), Finoguenov et al. (2002) and Matsushita et al. (2002). We assumed the distribution of gas to be spherically symmetric around M87 and restricted our consideration to the central region with a radius of 250 kpc. The electron density radial profile was represented by a sum of two beta models (9) with the following parameters: $N_0 = 0.13 \text{ cm}^{-3}$, $r_c = 1.7 \text{ kpc}$, $\beta = 0.42$ and $N_0 = 0.011 \text{ cm}^{-3}$, $r_c = 22 \text{ kpc}$, $\beta = 0.47$. For the temperature we adopted a constant value of $kT = 1 \text{ keV}$ within the central 1 kpc, the dependence $kT = 1.5(r/5 \text{ kpc})^{0.22} \text{ keV}$ between 1 and 50 kpc, and a constant value of 2.5 keV at larger radii. The last value approximately corresponds to temperatures measured with ASCA (Shibata et al. 2001) in different parts of the Virgo cluster within ~ 300 kpc from M87. The density and temperature profiles we use are shown in Fig. 8. The element abundances were taken to

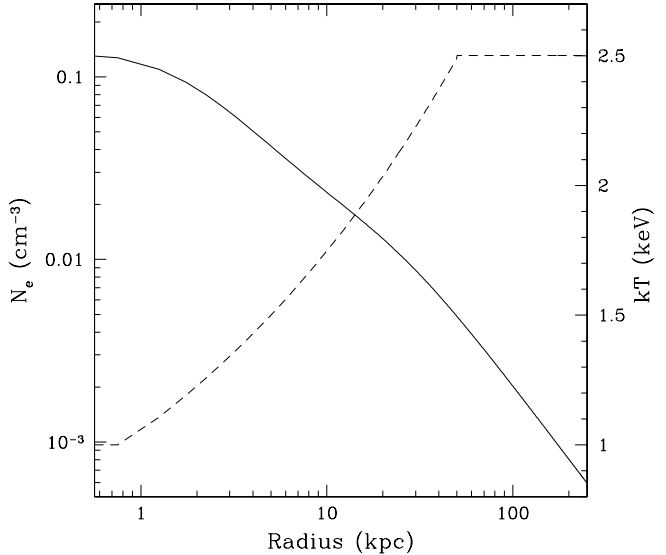


Fig. 8. Radial profiles of electron number density (the solid line) and temperature (the dashed line) representing the gas surrounding M87.

Table 1. The brightest X-ray and far UV resonance lines of the M87/Virgo intracluster gas.

Ion	Energy (keV)	Equivalent width (eV)	Optical depth
Fe XXIV	0.049	1	3.0
Fe XXIV	0.065	2	6.0
Fe XXIII	0.093	3	8.5
O VIII	0.654	20	0.6
Ne X	1.021	30	0.9
Fe XXIII	1.129	10	3.2
Fe XXIV	1.166	30	2.7
Si XIII	1.865	10	1.3
Si XIV	2.005	60	1.3
S XV	2.461	20	1.3
Ar XVII	3.140	20	0.4
Fe XXV	6.700	740	1.2
Fe XXV	7.881	110	0.2

be constant at $r < 10$ kpc, with $A(\text{O}) = 0.4$, $A(\text{Si}) = 1.0$, $A(\text{S}) = 1.0$, $A(\text{Ar}) = 1.0$ and $A(\text{Fe}) = 0.8$ (in units of solar abundances), then gradually declining to $A(\text{O}) = 0.4$, $A(\text{Si}) = 0.6$, $A(\text{S}) = 0.6$, $A(\text{Ar}) = 0.6$ and $A(\text{Fe}) = 0.4$ at $r = 40$ kpc, and constant thereafter.

Table 1 lists resonance X-ray lines (also included are lines with $E_{ik} \sim 50\text{--}100$ eV corresponding to $2s - 2p$ tran-

sitions in Fe XXIII and Fe XXIV) that are estimated to be the strongest emission lines of the M87 gas. All of these lines have substantial optical depths (from the center to the boundary of the gas cloud, assuming negligible turbulence).

Using equation (20), we can estimate for the stationary scenario the contribution of scattered AGN radiation to the surface brightness of M87/Virgo in the X-ray continuum:

$$\frac{B_{E,\text{cont}}^{\text{scat}}}{B_{E,\text{cont}}} = 4 \times 10^2 \frac{L_X}{L_{\text{Edd}}} E^{-1} \exp(E/1.5 \text{ keV}) \\ \times \left(\frac{\rho}{1.7 \text{ kpc}} \right)^{-0.7}, \text{ for } 1.7 \text{ kpc} \ll \rho \ll 22 \text{ kpc} \quad (30)$$

and

$$\frac{B_{E,\text{cont}}^{\text{scat}}}{B_{E,\text{cont}}} = 40 \frac{L_X}{L_{\text{Edd}}} E^{-1} \exp(E/2 \text{ keV}) \\ \times \left(\frac{\rho}{22 \text{ kpc}} \right)^{-0.6}, \text{ for } \rho \gg 22 \text{ kpc.} \quad (31)$$

Here we have used the fact that the density profile shown in Fig. 8 consists of two beta models, and assumed constant temperatures of $kT = 1.5 \text{ keV}$ and $kT = 2 \text{ keV}$ for equations (30) and (31), respectively. We also assumed $\alpha = 2$.

The corresponding dependences for the equivalent width of a resonance line with $\tau_0 \ll 1$ can be found from equations (30) and (31) as $\Delta EW/EW_0 = (R - 1)B_{E,\text{cont}}^{\text{scat}}(E_{ik})/B_{E,\text{cont}}(E_{ik})$ (assuming constant element abundances for a given ρ).

Now we proceed to discussing the results of our computations, which do not use the assumption of small optical depth.

4.1.1. Switch-off scenario

We first consider a scenario in which the central source in M87 was bright in the past for a long time (at least $\sim 1 \text{ million years}$) until it suddenly turned off (actually switched to its present low-luminosity state) at $t_{\text{off}} = 0$. We have plotted in Figs. 9 and 10 for two resonance lines the computed contribution of scattered radiation from the AGN to the surface brightness in the line as a function of projected radius as would be measured by observers living at various times $t > 0$ after the switch-off. Also shown are the corresponding profiles for the continuum emission at the energies of the resonance lines. The relative contribution of scattered AGN emission is a factor of $R \sim 6$ (with a scatter of ~ 3 between the lines) larger for the lines than for the continuum, in agreement with the main result of §2. We adopted the value $L_X = 0.01L_{\text{Edd}}$ for our examples. Since the discussed effect is proportional to L_X , the results can be easily recomputed for any AGN luminosity.

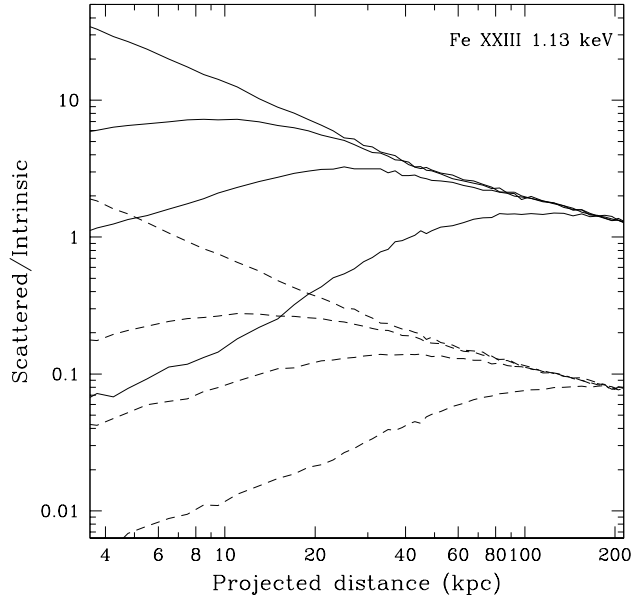


Fig. 9. Ratio of the surface brightness of scattered AGN radiation to the intrinsic brightness of the hot gas in the iron 1.13 keV resonance line, in the switch-off scenario for M87, at different times after the AGN switch-off as a function of projected radius. The AGN emitted $L_X = 0.01L_{\text{Edd}}$ in the past. The different solid curves correspond, from top to bottom, to elapsed times of 5, 50, 100 and 250 thousands years. The dashed lines show the corresponding profiles for the spectral continuum at the energy of the resonance line.

During the first \sim a few 10^4 years after the switch-off, a prominent peak in the scattered/thermal brightness ratio is observed near the nucleus. If we were fortunate to live during this period we could receive a significant flux of AGN radiation scattered by the core ($r \lesssim 22 \text{ kpc}$) towards us. Equation (30) gives a rough estimate of the resulting effect for $\rho \sim$ a few kpc for this early epoch. At later times, $t \gtrsim 5 \times 10^4$ years, the surface brightness drops sharply within the core region, while it remains practically unchanged in more distant regions for a long time $\sim \rho/c$ after the switch-off. This gives rise to the broad maxima of the scattered/thermal brightness ratio seen in Figs. 9 and 10.

The finite depth effects that were discussed in §3.3.1 play in the M87 case only a minor role for the X-ray lines because for them $\tau_0 < 3$ (see Table 1). Fig. 11 compares two cases, $M = 0$ (no turbulence) and $M = 0.5$ (significant turbulence), for the iron 1.13 keV line. The introduction of turbulence leads to a decrease from $\tau_0 = 3.2$ to $\tau_0 = 0.7$. We see that the relative contribution of scattered AGN emission to the surface brightness in the central

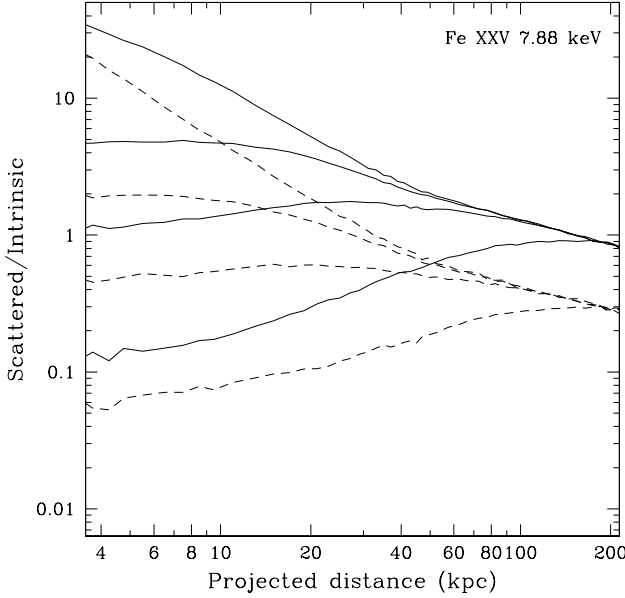


Fig. 10. Same as Fig. 9, but for the iron Fe 7.88 keV line.

~ 10 kpc is several times larger in the former (optically-thick) case, except for the early moments. This increase is mainly due to delayed escape of photons.

Fig. 12 compares the surface brightness profiles of scattered radiation from the AGN and thermal emission in the iron 6.7 keV line, which has the largest equivalent width in our sample. In an experiment one would hope to detect first of all scattered radiation from the region of maximum scattered/thermal brightness ratio (see Figs. 9 and 10), which is centered on $\rho_{\max} \sim ct$ and covers a projected area $S_{\max} \sim \rho_{\max}^2$. Important therefore are the fluxes of thermal and scattered radiation coming from this maximum zone. We can make a simple estimate for an isothermal gas. The surface brightness behaves as $B \propto \rho^{-6\beta+1}$ at $\rho \gg r_c$, hence the corresponding flux $F \sim S_{\max}B \propto \rho_{\max}^{-6\beta+3}$. The flux of scattered AGN radiation from the same region can be estimated as $F_{\text{scat}} \sim S_{\max}B_{\text{scat}} \propto \rho_{\max}^{-3\beta+1}$. In the case of M87, $F \propto \rho_{\max}^{0.2} \propto t^{0.2}$ [note that F is variable only because of the dependence $\rho_{\max}(t)$] and $F_{\text{scat}} \propto \rho_{\max}^{-0.4} \propto t^{-0.4}$, i.e. an almost constant flux of thermal emission and a slowly decreasing with time flux of scattered AGN radiation. Of course, the actual dependences will be somewhat different for individual lines because of the temperature and abundance radial variations in the M87 gas. Nevertheless, we see that the detector sensitivity threshold is not expected to impose strong restrictions on the prospects for observing scattered nuclear radiation in M87/Virgo, as well as in other clusters with similar slowly declining density profiles ($\beta \approx 0.5$).

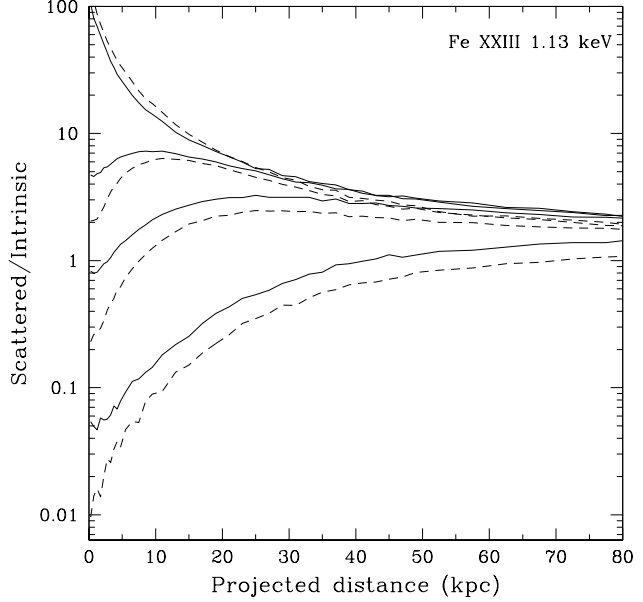


Fig. 11. Ratio of the surface brightness of scattered AGN radiation to the intrinsic brightness of the hot gas in the iron 1.13 keV resonance line, in the switch-off scenario for M87, as a function of projected radius. The sampled times are as in Figs. 9 and 10. The solid curves correspond to the case of negligible turbulence, and the dashed curves to $M = 0.5$. Note the linear scaling chosen for the projected radius, as opposed to the logarithmic scaling in Figs. 9 and 10.

We can now address the principal question of our study: what constraints can X-ray observations place on the past luminosity of the M87 central source? Suppose that it is possible in an experiment to map the distribution of the equivalent width of a particular line over M87/Virgo with $\delta = 10\%$ accuracy, which we consider a realistic value (see the discussion in §5). Then the following procedure can be suggested: if the relative contribution of scattered AGN emission exceeds δ at least at some projected radius (i.e. at least at the maximum of EW/EW_0 seen in Figs. 9 and 10), then we can estimate the past AGN luminosity. If no variation of the required amplitude is found, then we will be able to place an upper limit on L_X . Based on this criterion we can determine from the results of our computations how the minimum detectable past luminosity of M87 depends on the time passed after the switch-off. The resulting relationship is presented in Fig. 13.

We see that in order to have a 10% contribution of scattered radiation from the AGN whose luminosity in the past was $L_X = 10^{-4}L_{\text{Edd}} = 4 \times 10^{43} \text{ erg s}^{-1}$ (i.e. several hundreds times higher than the combined X-ray luminosity of the nucleus and jet now), we should live

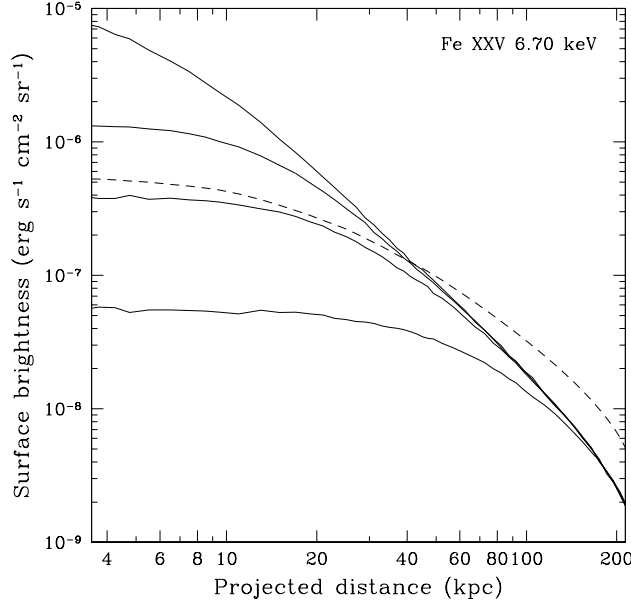


Fig. 12. M87/Virgo surface brightness of scattered AGN radiation (the solid lines) in the iron 6.70 keV resonance line at different times after the AGN switch-off. The dashed curve shows the intrinsic surface brightness profile of the hot gas in the 6.70 keV line, which also is distorted by resonant scattering. The AGN emitted $L_X = 0.01L_{\text{Edd}}$ in the past. The sampled times are as in Figs. 9–11.

not later than $\sim 3 \times 10^4$ years after the switch-off and look with X-ray telescopes into the M87 core region ($\rho \lesssim 10$ kpc ~ 2 arcmin in the plane of the sky), as is clear from Figs. 9 and 10. If the luminosity in the past was higher, $L_X = 10^{-3}L_{\text{Edd}} = 4 \times 10^{44} \text{ erg s}^{-1}$, we must live not later than $\sim 2 \times 10^5$ years after the switch-off and look further out (at $\rho \sim 50 - 200$ kpc ~ 20 arcmin from the AGN). The nearly flat shape of the curves in Fig. 13, which have been truncated at $t = 3 \times 10^5$ years to minimize the effects of the finite size of our model gas cloud, suggests that if the X-ray luminosity of the M87 nucleus was \sim a few $10^{-3}L_{\text{Edd}} \sim 10^{45} \text{ erg s}^{-1}$ in the past, the maximum allowed elapsed time would only be restricted by the extent of the gas in the Virgo cluster (~ 1 Mpc), the effective area of the detector and the field of view of the telescope.

There is a fairly small, less than a factor of 4, scatter between the curves in Fig. 13 corresponding to different spectral lines. It mainly arises due to the energy-dependent factor appearing in equation (31) and the different R values for different lines (see §2).

We may therefore conclude that it should be possible with future X-ray spectrometers to obtain fairly tight limits on (and possibly to measure) the past X-ray luminosity

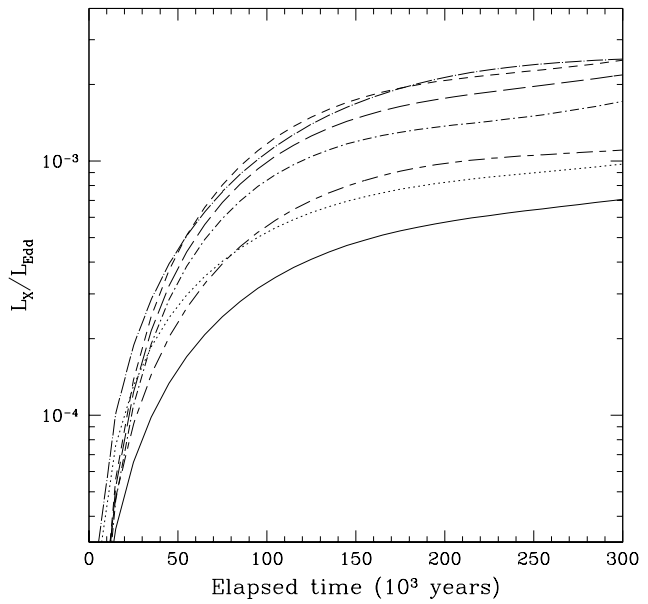


Fig. 13. Minimum detectable (as defined in the text) past X-ray luminosity as a function of elapsed time in the switch-off scenario for the M87 AGN. The different lines correspond to mapping M87/Virgo in different lines: Fe 1.13 keV line (solid), Fe 1.17 keV line (dotted), Si 1.86 keV line (short-dashed), S 2.46 keV line (long-dashed), Ar 3.14 keV line (dot-short-dashed), Fe 6.70 keV line (dot-long-dashed) and Fe 7.88 keV line (short-dash-long-dashed).

of the central source in M87. For comparison, we can use the available data of XMM-Newton observations of the M87 cooling flow region to obtain some weaker limits already now. Boehringer et al. (2001) have analyzed X-ray spectra taken from a sequence of rings centered on the M87 nucleus. The most distant ring has an outer radius $r_{\text{out}} \approx 60$ kpc, and the innermost circle has $r_{\text{in}} \approx 1.25$ kpc. Except for the spectrum of the central circle to which the direct emission from the AGN contributes, the individual spectra correspond to optically thin thermal emission from the gas. The quality of the spectra is apparently good up to an energy ~ 7 keV. We can therefore suggest that the surface brightness of scattered AGN radiation (having a power-law spectrum) does not exceed the actually measured surface brightness in the X-ray continuum at $E = 7$ keV nowhere between $\rho = 1.25$ kpc and 60 kpc. From this condition we can find an upper limit on the past X-ray luminosity of M87 as a function of time passed after the switch-off, similarly as we derived the limits presented in Fig. 13 based on the resonance line computations. Note, however, that in the previous case we did not impose any limitations on the projected radius and we

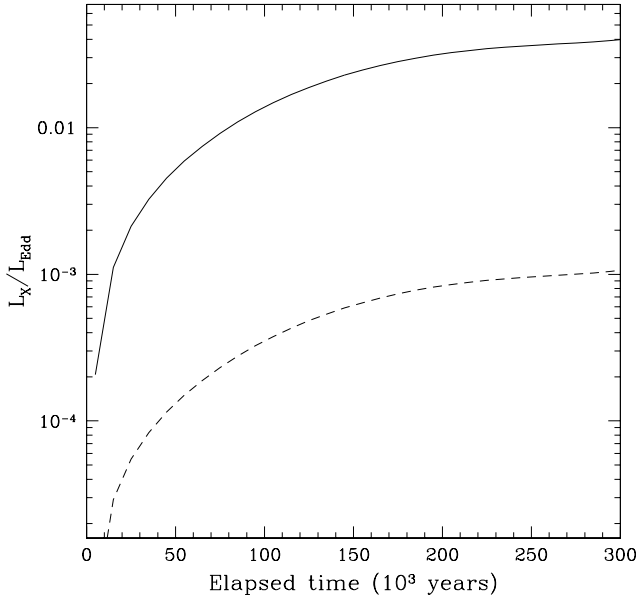


Fig. 14. Upper limit on the past X-ray luminosity of the M87 AGN as a function of elapsed time after the switch-off, obtained from the XMM-Newton observations of the M87 cooling flow in the X-ray spectral continuum up to $E = 7$ keV (the solid line). For comparison shown (the dashed line) are the limits that could be obtained if the thermal emission from the M87 gas could be detected up to $E = 15$ keV.

adopted a value $\delta = 10\%$, rather than $\delta = 100\%$ to be used now. The resulting dependence is shown in Fig. 14.

We see that the current limits based on the spectral continuum data are rather weak. For example, we can state that the average X-ray luminosity of the M87 AGN over a long period of $\gtrsim 10^5$ years ending 5×10^4 years ago was not higher than $5 \times 10^{-3} L_{\text{Edd}} = 2 \times 10^{45}$ erg s $^{-1}$. By comparing Fig. 14 and Fig. 13, we see that the current limits could be improved by at least an order of magnitude by means of fine X-ray spectroscopy. Alternatively, tighter limits could be obtained by measuring the surface brightness of M87/Virgo in the hard X-ray continuum. To illustrate this possibility, we have repeated our analysis for $E = 15$ keV – see the resulting dashed line in Fig. 14. Going from $E = 7$ keV to 15 keV leads to a factor of ~ 30 stronger limits. The hard X-ray telescope required for such observations must have arcminute angular resolution to probe elapsed times $\sim 10^5$ years.

4.1.2. Flare scenario

Suppose now that some time ago M87 experienced an outburst that was short compared to the characteristic light

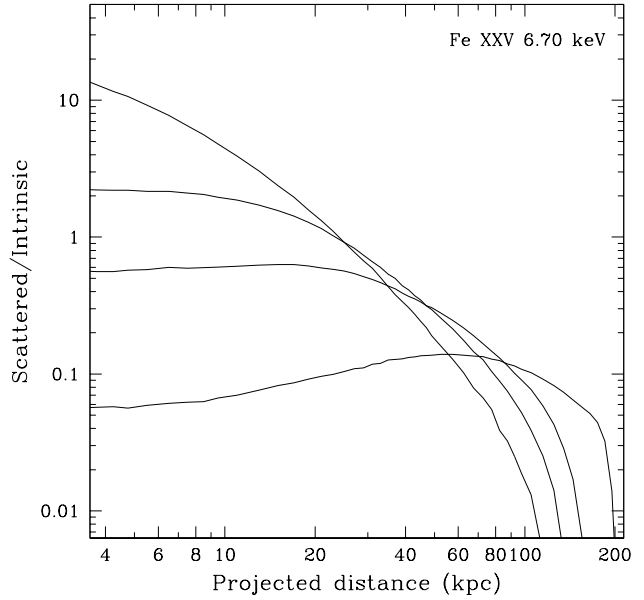


Fig. 15. Ratio of the surface brightness of scattered AGN radiation to the intrinsic brightness of the hot gas in the iron 6.70 keV resonance line, at different times after a 10^5 -year outburst as a function of projected radius. The AGN emitted $L_X = 0.01L_{\text{Edd}}$ during the flare. The different solid curves correspond, from top to bottom, to elapsed times of 5, 50, 100 and 250 thousands years.

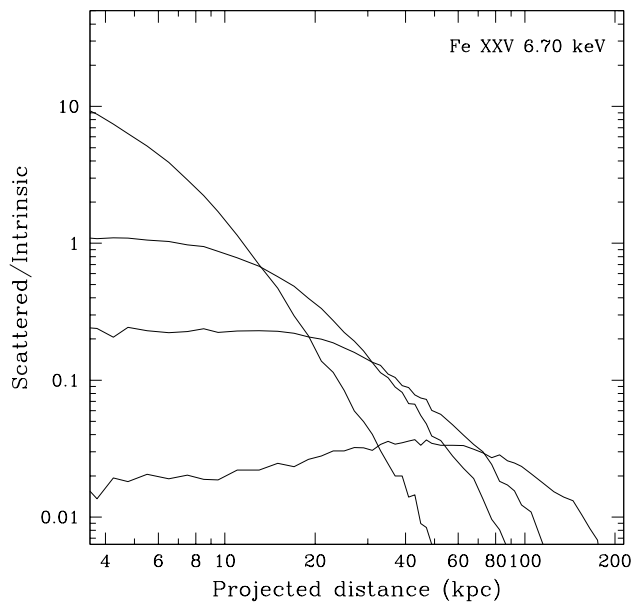


Fig. 16. Same as Fig. 15, but for a 2×10^4 -year outburst.

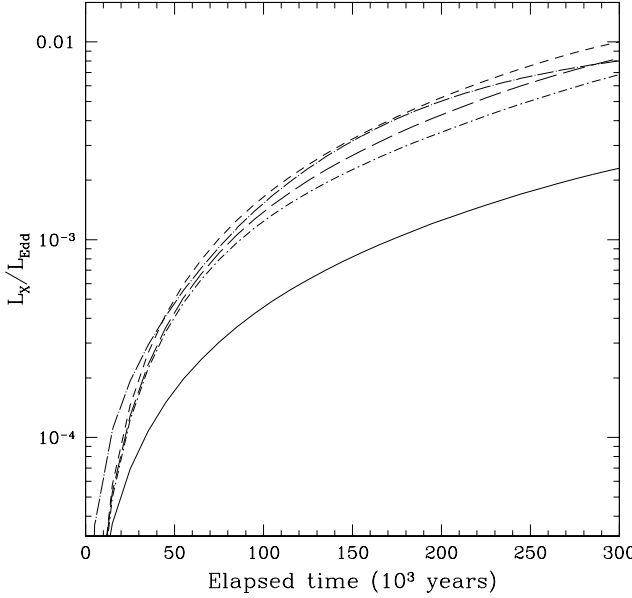


Fig. 17. Minimum detectable (as defined in the text) outburst X-ray luminosity as a function of elapsed time in the case of a 10^5 -year flare of the M87 AGN. The different lines correspond to mapping M87/Virgo in different lines: Fe 1.13 keV line (solid), Fe 1.17 keV (dotted), Si 1.86 keV (short-dashed), S 2.46 keV (long-dashed), Ar 3.14 keV (dot-short-dashed), Fe 6.70 keV line (dot-long-dashed) and Fe 7.88 keV line (short-dash-long-dashed).

crossing time of the gas cloud, i.e. $\Delta \ll 10^6$ years. Some analytic estimates for this case were obtained in §3.2.3. Figs. 15 and 16 show the computed time evolution of the scattered/thermal brightness ratio profile for the Fe XXV K α line for outburst durations $\Delta = 10^5$ years and $\Delta = 2 \times 10^4$ years, respectively, and an AGN luminosity $L_X = 0.01L_{\text{Edd}}$. Note that for $t \gg \Delta$ the scattered surface brightness profile depends on the product $L_X\Delta$, rather than on L_X and Δ separately.

Figs. 17 and 18 show the minimum detectable (for 10% scattered contribution) AGN outburst luminosity as a function of elapsed time for the two considered scenarios ($\Delta = 10^5$ and 2×10^4 years). These dependences should be compared with Fig. 13 representing the switch-off scenario. We see that until a certain moment $t_{\text{crit}} \sim \Delta$ the minimum detectable luminosity is only a little smaller in the flare case than in the switch-off case. This is expected, because the characteristic line-of-sight depth of the illuminated volume at $t = t_{\text{crit}}$ is about the same, $\delta\rho \sim ct_{\text{crit}}$, in both cases. Only at $t \gg \Delta$, does the minimum detectable luminosity become much larger (by a factor of Δ/t) for short outbursts. This directly follows from a comparison of equations (20) and (23).

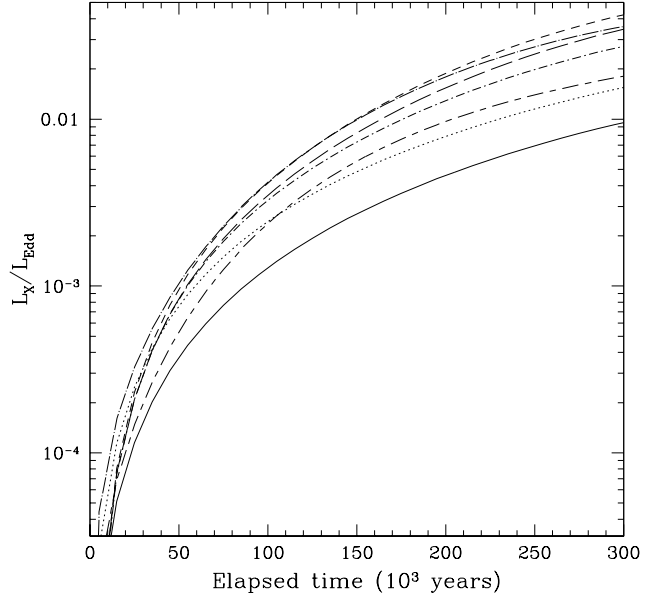


Fig. 18. Same as Fig. 17, but for a 2×10^4 -year long outburst.

For comparison, Fig. 19 shows upper limits for the same outburst scenarios but obtained using the XMM-Newton data on the X-ray continuum emission from the M87 cooling flow.

4.2. Cygnus A

Our second example is Cyg A. This is a well-known nearby ($z = 0.0562$, i.e. about 20 times more distant than M87 – 1 arcmin approximately corresponds to 100 kpc) powerful radio galaxy. Cyg A has recently been observed with the Chandra satellite, and detailed information was obtained on the morphology of X-ray emission from the galaxy (Young et al. 2002) as well on the intracluster gas surrounding it (Smith et al. 2002).

In the Chandra and quasi-simultaneous RXTE observations (Young et al. 2002), hard (up to 100 keV), spatially unresolved X-ray emission was detected from the position of the radio and infrared nucleus of Cyg A. The energy spectrum of this radiation is power law with photon index $\alpha = 1.5$, heavily absorbed at energies below a few keV. The inferred unabsorbed 1–10 keV luminosity of the nucleus $L_X \sim 5 \times 10^{44}$ erg s $^{-1}$. This is four orders of magnitude more than the X-ray luminosity of the M87 nucleus.

The Chandra observations clearly reveal an intracluster medium. The gas has complex structure within the central ~ 100 kpc, which apparently is the result of an interaction with the relativistic material produced by nu-

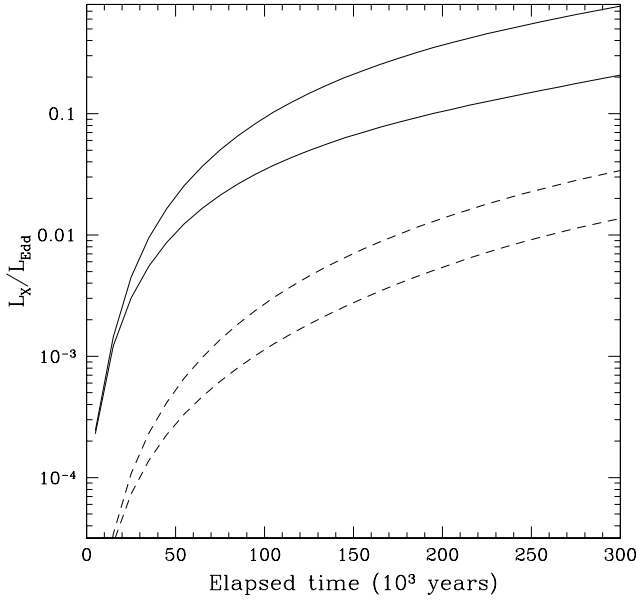


Fig. 19. Upper limit, as a function of elapsed time, on the X-ray luminosity of the M87 AGN during its 10^5 -year (lower solid line) or 2×10^4 -year (upper solid line) flare, obtained from the XMM-Newton observations of the M87 cooling flow in the X-ray spectral continuum up to $E = 7$ keV. For comparison shown (the dashed lines) are the limits that could be obtained if the thermal emission of the M87 gas could be measured up to $E = 15$ keV.

clear activity. In contrast, the morphology of the gas is simple at larger radii ($\gtrsim 100$ kpc), namely the gas appears to be spherical within at least 700 kpc from the nucleus, and nearly isothermal with $kT \sim 7 - 8$ keV. The total luminosity of the intracluster gas is about 10^{45} erg s^{-1} , which is comparable to the X-ray luminosity of the central AGN and is a typical value for rich clusters of galaxies.

Given the above observational facts, we can estimate the contribution of scattered emission from the AGN to the X-ray surface brightness outside the central 100 kpc of the Cyg A cluster. Due to the highly irregular distribution of gas in the innermost region of Cyg A, our simulations will not be aimed at this zone. Based on these considerations and the results of Smith et al. (2002), we model the radial distribution of gas density by a beta model with $N_0 = 0.05$ cm $^{-3}$, $r_c = 30$ kpc and $\beta = 0.5$. The temperature is assumed to be constant, $kT = 5$ keV, within the central 50 kpc and also at $r > 150$ kpc, $kT = 7.5$ keV, as shown in Fig. 20. The abundance of iron is taken to be 0.35 solar. Our model cloud of gas has an outer boundary at $r = 1$ Mpc.

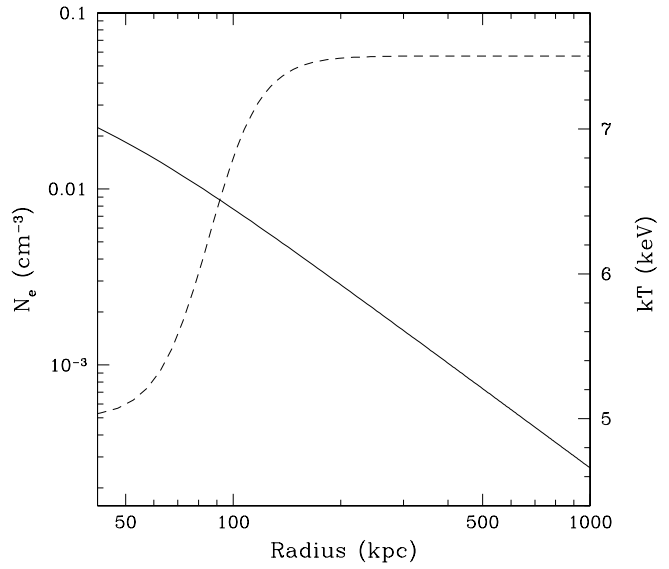


Fig. 20. Radial profiles of electron number density (the solid line) and temperature (the dashed line) representing the Cyg A intracluster gas.

Table 2. The brightest resonance X-ray and far UV lines of the Cyg A intracluster gas.

Ion	Energy (keV)	Equivalent width (eV)	Optical depth
Fe XXIV	0.049	1	0.9
Fe XXIV	0.065	2	1.8
Fe XXV	6.70	250	1.8
Fe XXV	7.88	40	0.3
Fe XXVI	6.97	200	0.3

Table 2 lists the strongest emission lines of the Cyg A cluster, as implied by our model. The X-ray lines include the K α and K β lines of He-like iron and the Ly α line of H-like iron. The Chandra and RXTE data do reveal two strong lines, one near 6.7 keV (Fe K α) and another near 7.9 keV (Fe K β plus possibly Ni K α). It appears (see Fig. 7 in Smith et al. 2002) that the measured (with moderate energy resolution) spectra also do not contradict the presence of a strong line at the position of Fe Ly α (6.97 keV).

We can estimate from equation (20) the stationary contribution of scattered AGN radiation to the surface

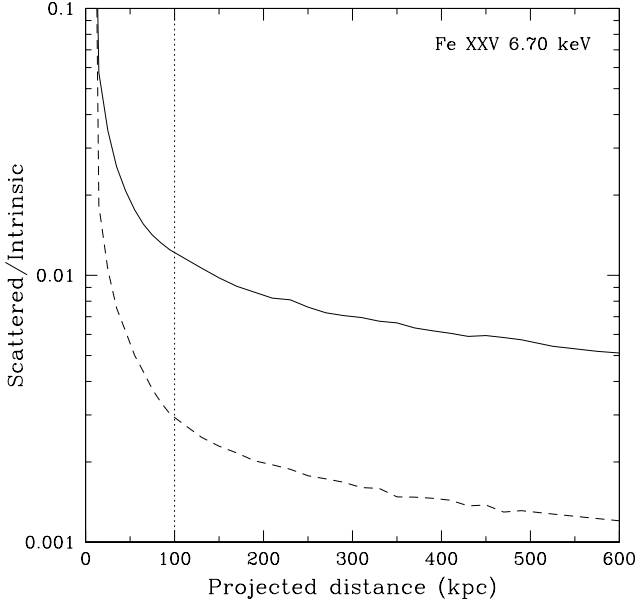


Fig. 21. Ratio of the surface brightness of scattered AGN radiation to the intrinsic brightness of the hot gas in the iron 6.70 keV resonance line, in the stationary scenario for Cyg A, as a function of projected radius (the solid line). The AGN X-ray luminosity is assumed to be equal to the present-day luminosity of the Cyg A nucleus, $L_X = 5 \times 10^{44} \text{ erg s}^{-1}$. The dashed line shows the corresponding profile for the spectral continuum at the energy of the resonance line. The vertical dotted line indicates that the results to the left of it are not reliable.

brightness of the Cyg A cluster in the X-ray continuum:

$$\frac{B_{E,\text{cont}}^{\text{scat}}}{B_{E,\text{cont}}} = 2 \times 10^{-3} \frac{L_X}{5 \times 10^{44} \text{ ergs}^{-1}} E^{-1/2} \exp(E/7.5 \text{ keV}) \times \left(\frac{\rho}{30 \text{ kpc}} \right)^{-0.5} \quad (32)$$

where we have normalized the X-ray luminosity of the Cyg A nucleus to its present-day value and used $\alpha = 1.5$.

Fig. 21 shows the computed Cyg A radial profile of the scattered/thermal surface brightness ratio for the iron 6.7 keV line, assuming that the nuclear X-ray luminosity has remained for a few millions years the same as it is now (the stationary scenario). We see that scattered AGN emission contributes of the order of 1% at $\rho \sim 200$ kpc. It then follows that the Cyg A luminosity should have been an order of magnitude higher in the past (i.e. $L_X \sim 5 \times 10^{45} \text{ erg s}^{-1}$) than it is now in order for scattered AGN radiation to contribute $\sim 10\%$ to the strong X-ray lines observed from the intracluster gas (see Fig. 22).

We can also use the available Chandra data on the X-ray continuum emission from the Cyg A cluster to find

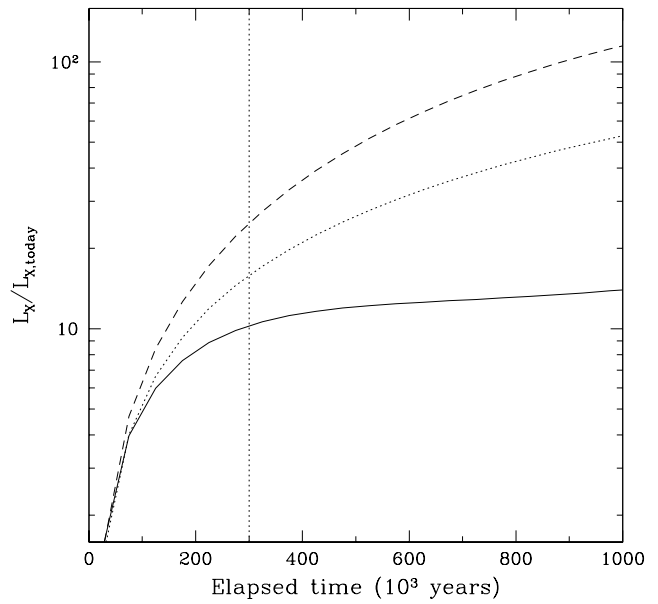


Fig. 22. Minimum detectable (as defined in the text) past X-ray luminosity of the Cyg A AGN as a function of elapsed time. The surface brightness is measured in the iron 6.70 keV line. The solid line corresponds to the switch-off case ($\Delta \rightarrow \infty$). The dotted and dashed lines correspond to outbursts of duration $\Delta = 5 \times 10^5$ years and $\Delta = 2 \times 10^5$ years, respectively. The luminosity is normalized to the present-day X-ray luminosity of the Cyg A nucleus. The vertical dotted line indicates that the results to the left of it are not reliable.

upper limits on the past X-ray luminosity of its central source. We adopt the following parameters for this analysis: $E = 8$ keV – the maximum photon energy at which thermal bremsstrahlung emission is still detected, and $\rho_{\min} = 10^2$ kpc and $\rho_{\max} = 6 \times 10^2$ kpc – the boundaries of the region that is well explored with Chandra. We plot the resulting upper limits in Fig. 23. We see that the current constraints are very weak because of the high temperature (~ 7 keV) of the intracluster gas. For comparison (see Fig. 23), with arcminute-resolution observations at $E \sim 40$ keV of the Cyg A cluster it could be possible to place limits on its past luminosity similar to those obtainable by means of fine X-ray spectroscopy (see Fig. 22).

5. Discussion

The results of the preceding sections indicate that the suggested method of constraining the past X-ray luminosity of galactic nuclei is promising. We have shown that there are two viable observational strategies. One is to

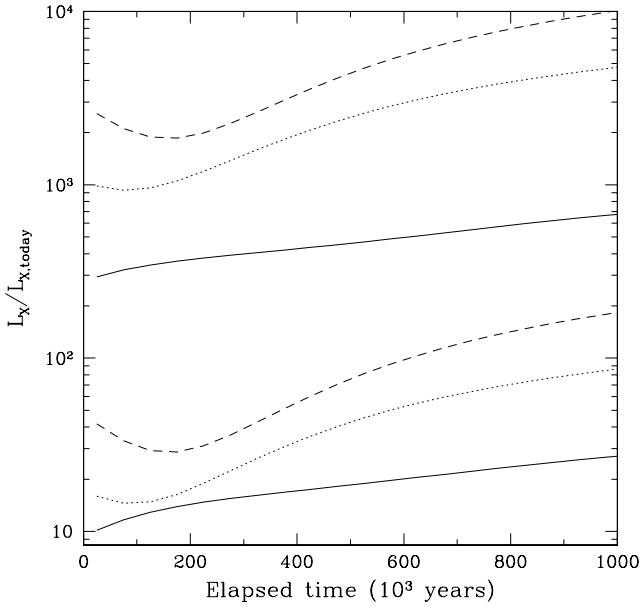


Fig. 23. Upper limit, as a function of elapsed time, on the X-ray luminosity of the Cyg A AGN either before a switch-off (upper solid line), or during a 5×10^5 -year outburst (upper dotted line) or during a 2×10^5 -year outburst (upper dashed line), obtained from the Chandra observations of the Cyg A cluster in the X-ray spectral continuum up to $E = 8$ keV. The luminosity is normalized to the present-day X-ray luminosity of the Cyg A nucleus. For comparison shown (the lower set of lines) are the limits that could be obtained if the thermal emission from the Cyg A cluster could be detected up to $E = 40$ keV.

search for traces of scattered AGN radiation in the spectral continuum at high energies $E \gg kT(1+z)$, and the other is to perform fine spectroscopic observations aimed at measuring the surface brightness of the hot gas in bright resonance X-ray lines. The first approach appears to be particularly promising for studying distant (at redshifts $z \gtrsim 0.5$) powerful quasars and their environments, whereas the second one is probably more appropriate for studying past nuclear activity in more nearby objects. Note that bright quasars may strongly photoionize the gas around them, so that there may be only weak line emission from such gas. This is an additional argument why observing in the X-ray continuum may be more suitable for constraining the lifetime of quasars and determining parameters of the surrounding gas.

Although we have been mostly discussing clusters of galaxies and their central dominant galaxies throughout the paper, the same method can also be applied to groups of galaxies and isolated giant elliptical galaxies, which also are large reservoirs of hot ionized gas capable of scattering

AGN radiation. The main advantage of clusters of galaxies is the larger extent of intracluster gas, which enables studying previous galactic activity on longer timescales (up to a few times 10^6 years for the richest clusters) than in the case of groups of galaxies and early-type galaxies (up to a few times 10^5 years). On the other hand, the latter two classes of object may prove favourable because typical gas temperatures for them are $kT \sim 1$ keV. Therefore, it can be possible to achieve a significant gain due to the factor $\exp(E/kT)$ by observing such objects at the standard X-ray band (< 10 keV). In particular, one can use the $\text{K}\alpha$ line of He-like iron at 6.7 keV. Indeed, the corresponding ions (Fe XXV) are still abundant at such low temperatures, but collisional excitation of the ions leading to emission in the line is already inefficient. We note, however, that due to the presence of unresolved satellites, the net gain from using the 6.7 keV line rather than low-energy resonance lines is not expected to be more than ~ 10 .

Although we have only considered the case where the AGN is an isotropic source, in reality angular anisotropy at some level is expected. For instance, we may expect symmetry of nuclear X-ray emission about the direction of a jet. Obviously, the distribution of scattered AGN emission will also be symmetric about this direction, a signature that can be searched for and would be an additional clear indication of the presence of the scattering effect. One consequence of such angular anisotropy is that the contribution of scattered emission from the AGN to the surface brightness can be larger in some parts of the gas than predicted assuming source isotropy based on the observed flux of X-ray emission coming directly from the AGN. This, for example, may affect our estimates made for the radio galaxies 3C294 and PKS 1138–262 in §3.2.2 and Cyg A in §4.2. We refer the reader to the papers by Gilfanov et al. (1987a) and Wise & Sarazin (1992) for a detailed discussion of scattered surface brightness profiles that may arise in the case of beamed source emission.

In the discussion of our simulations for the M87 and Cyg A galaxies and their associated clusters of galaxies we used a fiducial value of 10% as the minimum detectable contribution of scattered AGN emission to the surface brightness in a resonance line. We realize that significant efforts will be required to achieve this or better detection level in an actual experiment. The main difficulty is that the measured surface brightness is the integral of emission (thermal plus scattered) along a given line of sight, and there may be present gas with different temperatures and element abundances along this line of sight. Both types of variations will have effect on the equivalent line width. In principle it should be possible to determine and subtract the underlying temperature and abundance radial trends from a careful analysis of the spectral-imaging data. The remaining uncertainties are expected to be largest for cluster cooling flows, where both the gas temperature and element abundances vary significantly with radius, like for

example in the M87 case. On the other hand, this problem is not expected to be severe for regions outside the cores of clusters. For example, in the Cyg A cluster the gas appears to be nearly isotropic outside the central ~ 200 kpc (see Smith et al. 2002), while the equivalent width of the 6.7 keV iron emission line changes by only $\sim 10\%$ when the gas temperature varies by 0.5 keV around $kT \sim 7.5$ keV. Therefore, achieving the 10% detection level appears realistic.

It is clear that the potential of the method can be fully realized only when it is possible to resolve interesting resonance lines from neighbouring lines. Indeed, lines other than permitted resonance lines can contribute significantly to the intrinsic emission of the gas, but relatively less or not at all to the scattered AGN emission. Moreover, it is desirable that all important lines in blends be resolved, such as the permitted, intercombination and forbidden lines in the complex around the 6.7 keV (Fe XXV K α) line. Even a small contribution of scattered emission from the AGN could then be made manifest by comparing the surface brightness profiles measured in these lines. We are therefore looking forward to future high-energy astrophysics missions such as Astro-E2, Constellation-X and XEUS that will provide the required energy resolution (\sim a few eV).

Acknowledgements. SS acknowledges support from a Peter Gruber Foundation Fellowship. RS as a Gordon Moore Scholar thanks Caltech for hospitality during the completion of this paper. This research was partially supported by the Russian Foundation for Basic Research (projects 00-02-16681 and 00-15-96649) and by the program of the Russian Academy of Sciences "Astronomy (Nonstationary astronomical objects)".

References

Anders, E., & Grevesse, N., 1989, *Geochimica et Cosmochimica Acta*, 53, 197

Arnaud, M., & Rothenflug, R. 1985, *A&AS*, 60, 425

Arnaud, K.A., 1996, *Astronomical Data Analysis Software and Systems V*, eds. Jacoby G. and Barnes J., ASP Conf. Series volume 101, 17

Bahcall, J.N., Kirhakos, S., Saxe, D.H., & Schneider, D.P., 1997, *ApJ*, 479, 642

Böhringer, H., Belsole, E., Kennea, J., Matsushita, K., Molendi, S., Worrall, D. M., Mushotzky, R.F., Ehle, M., Guainazzi, M., Sakelliou, I., Stewart, G., Vestrand, W.T., & Dos Santos, S. 2001, *A&A*, 365, 181

Boyce, P.J., Disney, M.J., Blades, J.C., Boksenberg, A., Crane, P., Deharveng, J.M., Macchetto, F.D., Mackay, C.D., & Sparks, W.B., 1997, *MNRAS*, 298, 121

Burderi, L., King, A.R., & Szuszkiewicz 1998, *ApJ*, 509, 85

Carilly, C.L., Harris, D.E., Pentericci, L., et al., 2002, *ApJ*, 567, 781

Cavaliere, A. & Fusco-Femiano, R. 1976, *A&A*, 49, 137

Chandrasekhar, S., 1950, *Radiative Transfer*, Oxford, Clarendon Press

Ciotti, L., & Ostriker, J.P. 2001, *ApJ*, 551, 131

Cramphorn, C.K., & Sunyaev, R.A. 2002, *A&A* (in press)

Crawford, C.S., Lehmann, I., Fabian, A.C., Bremer, M.N., & Hasinger, G., 1999, *MNRAS*, 308, 1159

Fabian, A.C., Crawford, C.S., Ettori, S., & Sanders, J.S., 2001, *MNRAS*, 322, L11

Fang, T.D., Davis, D.S., Lee, J.C., Marshall, H.L., Bryan, G.L., & Canizares, C.R., 2002, *ApJ*, 565, 86

Finoguenov, A., Matsushita, K., Böhringer, H., Ikebe, Y., Arnaud, M., 2002, *A&A*, 381, 21

Gilfanov, M.R., Sunyaev, R.A., & Churazov, E.M. 1987a, *Sov. Astron. Lett.*, 13, 233

Gilfanov, M.R., Sunyaev, R.A., & Churazov, E.M. 1987b, *Sov. Astron. Lett.*, 13, 3

Hardcastle, M.J., & Worrall, D.M., 1999, *MNRAS*, 309, 969

Harris, D.E., Nulsen, P.E.J., Ponman, T.J., Bautz, M., Cameron, R.A., David, L.P., et al., 2000, *ApJ*, 530, L81

Hardcastle, M.J., Birkinshaw M. & Worrall D.M., 2001, *ApJ*, 323, L17

Hernquist, L. 1989, *Nature*, 340, 687

Hooper, E.J., Impey, C.D., & Foltz, C.B., 1997, *ApJ*, 480, L95

Kaastra, J.S., 1992, *An X-Ray Spectral Code for Optically Thin Plasmas* (Internal SRON-Leiden Report, updated version 2.0)

Kallman, T.R., & McCray, R., 1982, *ApJ*, 50, 263

Kirhakos, S., Bahcall, J.N., Schneider, D.P., & Kristian, J., 1999, *ApJ*, 520, 67

Lidzkii, V.V., & Ozernoi, L.M., 1979, *Sov. Astron. Lett.* 5, 16

Liedahl, D.A., Osterheld A.L. and Goldstein W.H., 1995, *ApJL*, 438, 115

Lin, D.N.C., & Shields, G.A. 1986, *ApJ*, 305, 28

Macchetto, F.D., Marconi, A., Axon, D.J., Capetti, A., Sparks, W.B., & Crane, P. 1997, *ApJ*, 489, 579

Marconi, A., Axon, D.J., Macchetto, F.D., Capetti, A., Sparks, W.B., & Crane, P. 1997, *MNRAS*, 289, L21

Matsushita, K., Belsole, E., Finoguenov, A., & Boehringer, H. 2002, *A&A* (in press); *astro-ph/0201242*

McLure, R.J., Kukula, M.J., Dunlop, J.S., Baum, S.A., O'Dea, C.P., & Hughes, D.H., 1999, *MNRAS*, 308, 377

McLure, R.J., & Dunlop, J.S., 2001, *MNRAS*, 321, 515

Mewe, R., Gronenschild, E.H.B.M. & van der Oord, G.H.J. 1985, *A&AS*, 62, 197

Mewe, R., Lemen, J.R., & van den Oord G.H.J., 1986, *A&AS*, 65, 511

Mineshige, S., & Shields, G.A., 1990, *ApJ*, 351, 47

Murphy, B.W., & Chernoff, D.F., 1993, *ApJ*, 418, 60

Owen, F.N., Eilek, J.A., & Kassim, N.E., 2000, *ApJ*, 362, 449

Rees, M.J. 1988, *Nature*, 333, 523

Reynolds, C.S., Di Matteo, T., Fabian, A.C., Hwang, U., & Canizares, C.R. 1996, *MNRAS*, 283, 111

Reynolds, C.S., Heinz, S., Fabian, A.C., & Begelman, M.C. 1999, *ApJ*, 521, 99

Sarazin, C.L., & Wise, M.W., 1993, *ApJ*, 411, 55

Schade, D.J., Boyle, B.J., & Letawsky, M., 2000, *MNRAS*, 315, 498

Shibata, R., Matsushita, K., Yamasaki, N.Y., Ohashi, T., Ishida, M., Kikuchi, K., Boehringer, H., & Matsumoto, H., 2001, *ApJ*, 549, 228

Sholomitskii, G.B. & Yaskovich, A.L., 1990, *Sov. Astron. Lett.*, 16, 383

Siemiginowska, A., Czerny, B., & Kostyunin, V., 1996, *ApJ*, 458, 491

Smith, D.A., Wilson, A.S., Arnaud, K.A., Terashima, Y., & Young, A.J., 2002, *ApJ*, 565, 195

Sunyaev, R.A. 1982, Sov. Astron. Lett., 8, 175

Sunyaev, R.A., Markevitch, M., & Pavlinsky M. 1993, ApJ, 407, 606

Tarter, C.B., & Tucker, W., & Salpeter, E.E., 1969, ApJ, 156, 943

Verner, D.A., & Ferland, G.J., 1996, ApJS, 103, 467

Verner, D.A., Verner, E.M., & Ferland, G.J., 1996, Atomic Data and Nuclear Data Tables, 64, 1

Wilson, A.S., & Yang, Y. 2002, ApJ, 568, 133

Wise, M.W., & Sarazin, C.L. 1990, ApJ, 363, 344

Wise, M.W., & Sarazin, C.L. 1992, ApJ, 395, 387

Worrall, D.M., Birkinshaw, M., Hardcastle, M.J., & Lawrence, C.R., 2001, MNRAS, 326, 1127

Yaqoob, T. & Serlemitsos, P., 2000, ApJ, 544, L95

Young, A.J., Wilson, A.S., Terashima, Y., Arnaud, K.A., & Smith, D.A., 2002, 564, 176

Zombeck, M.V. 1990, Handbook of Astronomy and Astrophysics, Second Edition (Cambridge, UK: Cambridge University Press)